Chapter 2
Background Physics

In this chapter I will introduce the theoretical concepts and experimental data that are relevant to the study of $Sr_3Ru_2O_7$ presented in this thesis. From a theoretical point of view the fundamental phenomena of a wide class of correlated electron systems are surprisingly well described by a non-interacting 'Fermi gas' theory. One of the first assumptions of this theory is not to take into account any electron–electron interactions besides Pauli's Exclusion Principle. It is thanks to a theory by Landau [1–3] that we understand why the results for the Fermi gas also apply qualitatively to strongly interacting Fermi liquids. Since the properties of the metallic ground state of $Sr_3Ru_2O_7$ in zero magnetic field are well described by the concepts of Landau's Fermi liquid theory I will review its most important results in the first part of this chapter. Indeed the predictions of Landau's Fermi liquid theory are so robust that it is in particular the systems that go beyond that theory and show non-Fermi liquid behaviour that have attracted a wealth of experimental and theoretical, with the high temperature superconductors of the cuprate [4] and recently iron–pnictide families [5] being but two of the most famous examples. In particular, the concept of quantum criticality has been used experimentally as a route to novel quantum states and will be briefly discussed.

The second part of this chapter will review the most relevant experimental data existing to date on $Sr_3Ru_2O_7$. Here I will in particular discuss the thermodynamic evidence for a metamagnetic quantum critical end point as well as the existence of a novel quantum phase in its vicinity. The chapter will finish with a summary of the experimental evidence for Fermi liquid quasiparticle excitations across the phase diagram.

2.1 Itinerant Electron Systems

To give a thorough introduction to the 'Fermi gas' or Landau's Fermi liquid theory is beyond the scope of this thesis. However, in order to put the experimental results

A. W. Rost, *Magnetothermal Properties near Quantum Criticality in the Itinerant Metamagnet $Sr_3Ru_2O_7$*, Springer Theses, DOI: 10.1007/978-3-642-14524-7_2,

and their significance into perspective it is necessary to summarise the most relevant results of the non-interacting theory in the first part of this section. Here particular emphasis will be put on the properties in magnetic fields. This will be followed by a basic introduction to Fermi liquid theory in order to show which concepts form the basis for its successful description of a wide range of itinerant electron systems. For more detailed discussions and derivations of the results presented here the books by Ashcroft and Mermin [6] for the properties of solid state systems in general and by Abrikosov et al. [7] for Landau Fermi liquid theory in particular give a good treatment of the subject and provide further references to the literature.

2.1.1 Non-Interacting Electron Theory

Many metals share a range of similar properties such as a linear temperature dependence of the specific heat at low temperatures. A very important step in understanding the generality of the physical laws applying to a vast range of different materials was Sommerfeld's theory of non-interacting fermionic particles that are constrained by boundary conditions in space. In combination with the study of the effect of a spatially varying periodic lattice potential on these non-interacting fermions, the theory is very successful in explaining many aspects of the properties of crystalline materials, especially at low temperatures. For the discussion in the following sections it is important to review the key concepts and nomenclature used.

The first concepts to mention are those of lattice momentum and the Brillouin zone. Since the periodic potential of the lattice destroys the continuous translational symmetry of real space, momentum is no longer a good quantum number. However, a crystalline system still retains a discrete translational symmetry leading to the definition of a lattice momentum. For the purposes here, one can—with one important exception—treat this lattice momentum the same way as the normal momentum, and the explicit reference to the lattice will be omitted in the reminder of the thesis. The important exception is that the momentum space is finite and can be confined to the first Brillouin zone, the primitive unit cell of the reciprocal lattice related to the real lattice via a Fourier transform. Under these conditions it is possible to show that the resulting single-electron energy–momentum dispersion in a crystalline solid is given by a series of energy bands $\epsilon_N(\mathbf{k})$ in the Brillouin zone. Here ϵ is the energy, $\mathbf{k}$ the momentum vector and N the band index. If one neglects the Coulomb and magnetic interaction between the electrons then these energy levels are occupied at zero temperature according to Pauli's Exclusion Principle up to a maximum energy, the so called Fermi energy ϵ_F. Each energy level is doubly occupied due to the degeneracy in spin space. It can be shown that in the thermodynamic limit ϵ_F is independent of sample size. These concepts are illustrated in Fig. 2.1 for the example of copper [6, p. 289].

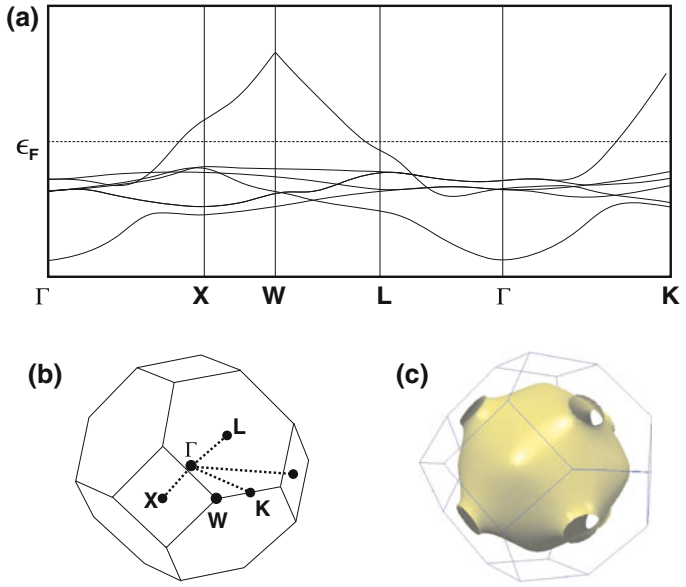

Fig. 2.1 **a** The band structure of Cu close to the Fermi energy ϵ_F is shown (graphic based on [6, p. 289]). The bands are plotted along lines in momentum space connecting points of high symmetry in the Brillouin zone. The position of these points is indicated in **b**, where the first Brillouin zone of Cu is given. The Fermi surface of Cu is shown in **c** [8, 9]

The wave vector in momentum space describing the Fermi surface is called the Fermi momentum $\mathbf{k}_F$. The Fermi surface topology is in general complicated. In particular, more than one band usually crosses the Fermi energy, giving a number of disconnected Fermi surfaces.

Most results of the theory take their simplest form for spherical Fermi surfaces. The magnitude of the Fermi momentum, k_F, is for example independent of direction and equal to the radius. For this reason mathematical results in this thesis are often presented for isotropic Fermi surfaces only. However, these are generally extendable to more complicated topologies.

The elementary excitation of such a system is the occupation of an unfilled level with an electron from a filled level. Whenever an electron crosses the Fermi energy a 'hole' is left behind in the states below the Fermi energy. The resulting symmetry in the number of particle and hole excitations is a fundamental property of a fermionic system as considered here. The typical width in energy of the electronic bands is of several eV. Therefore, any measurement of the system involving energy scales of not more than a few meV probes the physics of the energy–momentum dispersion close to the Fermi surface. As a result many properties of the system can be written in terms of a linearised band structure at ϵ_F. In connection to this an important quantity is the density of states $g(\epsilon)$, with $g(\epsilon)\mathrm{d}\epsilon$ giving the number of electronic states in the energy range from ϵ to $\epsilon + \mathrm{d}\epsilon$ normalised by the sample volume V.

An important class of measurements are thermodynamic experiments at low temperature. Since a temperature of 10 K corresponds to an average thermal energy of the order of 1 meV the above assumption of linearisation is often fulfilled experimentally. In this limit the electronic specific heat c_{el} is linear in temperature T and given by

$$c_{el} = \frac{\pi^2}{3} k_B^2 T g(\epsilon_F), \tag{2.1}$$

with k_B being Boltzmann's constant. The factor $(\pi^2/3)k_B^2 g(\epsilon_F)$ is called Sommerfeld coefficient γ. In the case of an isotropic surface, γ can be written as

$$\gamma = \frac{k_B^2}{3} k_F^2 \left(\frac{\partial \epsilon}{\partial k}\bigg|_{k_F} \right)^{-1}. \tag{2.2}$$

Comparing this result to the Sommerfeld coefficient of the free electron gas,

$$\gamma_{gas} = \frac{m_e k_B^2}{3\hbar^2} k_F, \tag{2.3}$$

leads to the definition of the thermodynamic effective mass m^* as

$$m^* = \hbar^2 k_F \left(\frac{\partial \epsilon}{\partial k}\bigg|_{k_F} \right)^{-1}. \tag{2.4}$$

A second class of experiments such as resistivity measurements or the response to strong magnetic fields involves dynamic properties of the electronic states. An appropriate theoretical framework for a discussion of most of the observed effects is the semiclassical theory. The basic components of this theory are electronic wavepackets in real space that represent an excitation of spin 1/2 and charge $-e$ being spread out over several lattice sites. If the analysis does not require too localised a wave function in real space, then one can represent it as a superposition of only a small number of momentum eigenstates around an average Fermi momentum $\mathbf{k}_F$. If one assumes furthermore that the applied electric or magnetic field is varying only slowly over the width of the wave packet, then it is possible to treat the field effectively as a classical force acting on the centre of the wave packet. The above described hierarchy of scales is shown schematically in Fig. 2.2.

An important variable in this theory is the (group) velocity of the wavepacket with which its centre of mass moves. It is given by

$$\mathbf{v}(\mathbf{k}) = \frac{1}{\hbar} \frac{\partial \epsilon}{\partial \mathbf{k}}, \tag{2.5}$$

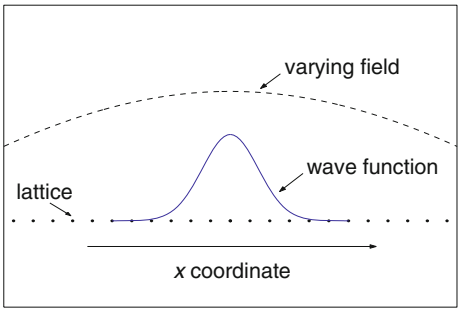

Fig. 2.2 This figure gives a overview of the hierarchy of scales in real space for which the semiclassical description is appropriate. The electron wavepacket described (*blue*) can only be localised to within several lattice site (*black dots*). Furthermore, the variations of the applied field have to be small on the scale of the wavepacket

with $\hbar$ being Planck's constant. The comparison of the momentum $\mathbf{p}$ of a wavepacket given by

$$\mathbf{p} = \hbar\mathbf{k}, \tag{2.6}$$

with the definition $\mathbf{p} = m^*\mathbf{v}$ for the classical momentum leading to a definition of an effective dynamic mass m^* as

$$m^* = \hbar^2 k_F \left(\left. \frac{\partial \epsilon}{\partial \mathbf{k}} \right|_{k_F} \right)^{-1}. \tag{2.7}$$

Note here that this is the same definition as has been obtained previously for the thermodynamic effective mass and no distinction between the two will be made in the following.

Within the semiclassical model one can derive the equations of motion for the position $\mathbf{r}$ and momentum $\mathbf{k}$ of a wavepacket under the influence of an electric field $\mathbf{E}$ and a magnetic field $\mathbf{H}$ as

$$\dot{\mathbf{r}} = \mathbf{v} = \frac{1}{\hbar} \left. \frac{\partial \epsilon}{\partial \mathbf{k}} \right|_{\mathbf{k}_F}, \tag{2.8}$$

$$\hbar\dot{\mathbf{k}} = -e\left[\mathbf{E} + \frac{1}{c}\mathbf{v} \times \mathbf{H} \right]. \tag{2.9}$$

Here e is the charge of an electron and c is the velocity of light.

After having introduced the fundamental concepts of the theory of a non-interacting Fermi gas I will in the following discuss its results regarding the effects of magnetic and electric fields in more detail.

2.1.2 Magnetic Field Effects

Magnetic field effects are generally treated in two regimes. In the first, one assumes that the dynamics of electrons due to the applied field, i.e. electron orbital effects, are negligible. An example for this limit is Pauli paramagnetism. The second case takes full account of the orbital motion leading to such effects as quantum oscillations.

2.1.2.1 Pauli Paramagnetism and an Extension Thereof

If a magnetic field $\mu_0 H$ is applied to an itinerant paramagnetic electron system then each electron can orient its spin parallel ($\uparrow$) or antiparallel ($\downarrow$) to the magnetic field.

Since orbital motion of the electrons will be neglected here the only effect of the field is a shift of the energy levels for the spin-up and spin-down electrons by $\pm\ \mu_B H$. Therefore, in the presence of the magnetic field the density of states for each species of electrons can be given in terms of the zero field density of states $g(\epsilon)$ by

$$g_{\uparrow/\downarrow}(\epsilon) = \frac{1}{2} g(\epsilon \mp \mu_B \mu_0 H). \tag{2.10}$$

The requirement of conservation of number of electrons N in the system then defines implicitly the Fermi energy ϵ_F at zero temperature via

$$N = \int_{-\infty}^{\epsilon_F} \left(g_\uparrow + g_\downarrow\right) \mathrm{d}\epsilon. \tag{2.11}$$

In the limit where the magnetic field is small, one can assume that the density of states is effectively constant, resulting in the Fermi energy ϵ_F being field independent. Furthermore, the magnetization M is given in terms of the number of spin up electrons, $n_\uparrow$, and spin-down electrons, $n_\downarrow$, by

$$M = -\mu_B (n_\uparrow - n_\downarrow) = -\mu_B (-\mu_B \mu_0 H g(\epsilon_F)), \tag{2.12}$$

resulting in the familiar expression for the susceptibility of Pauli paramagnetism χ of

$$\chi = \mu_B^2 g(\epsilon_F). \tag{2.13}$$

Two things should be mentioned. First of all the derivation at no point made any reference to the band structure other than the density of states, nor to the orientation of the magnetic field. Pauli paramagnetism is therefore isotropic. Furthermore, for simplicity, the argument was presented only for zero temperature, but it can be shown that χ is, to first order, temperature independent.

The reason the effect was presented in some detail here is because in the following it will be discussed what occurs when the magnetic field is sufficiently strong such that the assumption of the constant density of states breaks down (however orbital effects will still be neglected). This, for example, can happen at experimentally accessible fields if there is a peak in the density of states close to the zero field Fermi energy. This thought experiment is presented in Fig. 2.3.

In part (a), a possible situation in zero magnetic field ($H_0 = 0$) is shown. Here the density of states $g_{\uparrow/\downarrow}(\epsilon)$ are shown as a function of energy for the spin-up (blue) and spin-down (red) electrons. The density of states has a peak below the Fermi energy ϵ_F at the energies $\epsilon_{c\uparrow}/\epsilon_{c\downarrow}$ which are identical in zero field. If one now applies a magnetic field H_1 (part b) the energy of the spin-up band is lowered whereas the energy of the spin-down band is increased. However, whereas the difference in shift between the two bands is given by $\mu_B H$, the

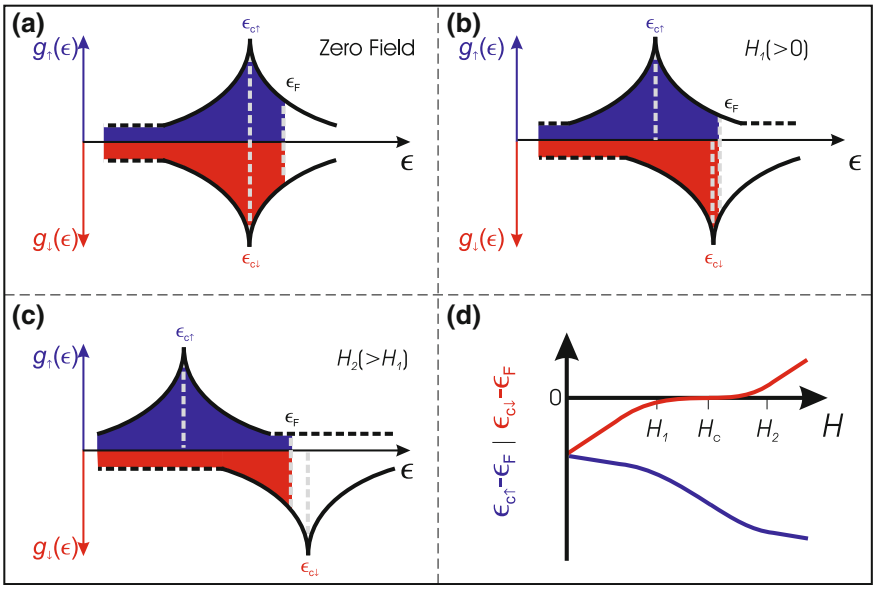

Fig. 2.3 Schematic representation of the effect of a magnetic field on the shift in the density of states of the spin up $(g_\uparrow(\epsilon))$ and spin down $(g_\downarrow(\epsilon))$ Fermi surfaces neglecting orbital effects. In zero magnetic field, as shown in **a**, the density of states of both spin species are the same. In the particular scenario here both density of states have a peak at $\epsilon_{c\downarrow}$ and $\epsilon_{c\uparrow}$ below the Fermi energy ϵ_F. The *filled states* of the two spin species are shown in *blue* (spin-up) and *red* (spin-down). In **b** and **c** it is shown that, when applying successively larger magnetic fields H_1 and H_2, the bands shift relative to each other with the density of states peak of one of the spin species being pushed through the Fermi energy. As discussed in the text the condition of overall number conservation causes the rate of change of the density of states to be a nonlinear function of applied field. This is shown schematically in **d** where the distance in energy of each of the density of states peaks from the Fermi energy ϵ_F, i.e. $\epsilon_{c\uparrow} - \epsilon_F$ and $\epsilon_{c\downarrow} - \epsilon_F$, is given as a function of magnetic field. As shown, $\epsilon_{c\uparrow} - \epsilon_F$ and $\epsilon_{c\downarrow} - \epsilon_F$ are not a linear function of $H - H_C$ where H_C is the critical field at which the peak in the density of states of one of the spin species crosses the Fermi energy

individual relative shift with respect to the Fermi energy is determined by number conservation. The consequence of this is that when the Fermi energy in one of the spin subspecies gets close to a peak in the density of states then the rate at which the Fermi energy approaches the peak as a function of applied magnetic field will slow down.

At a sufficiently high magnetic field the Fermi energy will have crossed the peak in the density of states as shown in Fig. 2.3c. Some careful remarks are necessary here. First, the above discussion completely ignores electron–electron interaction effects. Secondly, here the orbital effects of electronic states, leading for example to the phenomenon of quantum oscillations [10], were neglected. Overall one would not expect necessarily to be able to make quantitatively correct predictions based on this 'Gedankenexperiment'. However, one main qualitative conclusion is expected to hold. Close to a density of states peak one cannot expect that the distance in energy of the Fermi energy to that peak, i.e. $(\epsilon_C - \epsilon_F)$, is directly proportional to $(H - H_C)$, which is the difference of the magnetic field H to the critical magnetic field H_C at which the Fermi energy would lie at the maximum of the density of states peak. This is shown explicitly in Fig. 2.3d, where the relation between the two is shown for the particular scenario discussed here.

2.1.2.2 Quantum Oscillations

In the previous section it was assumed that the only coupling to the magnetic field is via the spin of the electrons. However, according to the semiclassical model introduced earlier, there exists a coupling between the magnetic field **H** and the momentum **k** of an electron wavepacket:

$$\hbar\dot{\mathbf{k}} = -e\left[\frac{1}{c}\mathbf{v} \times \mathbf{H}\right]. \tag{2.14}$$

On closer inspection of this equation one finds that the trajectory of the wavepacket in momentum space is along a path of constant energy in a plane perpendicular to the applied magnetic field **H**. In other words, if the wavepacket originates at the Fermi surface its trajectory is a trace along the Fermi surface in a plane perpendicular to the magnetic field. In the following it will be assumed for simplicity that the plane in which the motion takes place in momentum space is the $k_x - k_y$ plane. One consequence of this is that k_x and k_y are not good quantum numbers any more.[1]

In suitable Fermi surface topologies the path of the electron will be closed, resulting in a motion in momentum space and real space that is periodic. Similarly

[1] They are replaced for a spherical Fermi surface by $(k_x \pm \mathrm{i}k_y)$.

to the situation of electronic orbits in atomic physics it follows that the motion has to satisfy a quantisation condition which can be expressed in terms of the area a enclosed in momentum space and an integer n as

$$a = \left(n + \frac{1}{2}\right)\frac{2\pi eH}{c\hbar}. \tag{2.15}$$

The above relation is known in the literature as Onsager's relation [11]. A consequence of it is that the eigenstates in momentum space now are lying on tubes (called Landau tubes) whose principle axis is determined by the direction of the magnetic field.

Since the radius of these tubes and, as can be shown, their degeneracy, changes with magnetic field, one expects the properties of the electronic system to vary as a function of field as well. The energy of each tube associated with a definite quantum number n has to vary as a function of field, leading to the the Landau tubes crossing the Fermi energy one by one. This leads to an oscillatory behaviour in the properties of the material that, as can be derived from the quantisation condition, is periodic in $1/H$. A detailed derivation of that dependence is given for example in the book by Shoenberg [10]. Here, I will summarise the main results in the limit of high quantum numbers n.

The first quantity which has to be affected is the density of states. The oscillatory component $\tilde{g}(\epsilon_F)$ of the total density of states $g(\epsilon_F)$ at the Fermi energy ϵ_F as a function of magnetic field H is proportional to [10]

$$\tilde{g}(E_F) \propto \left(\frac{eH}{c\hbar}\right)^{1/2} m^* \sum_{p=1}^{\infty} \frac{1}{p^{1/2}} \cos\left(2\pi p\left(\frac{Ac\hbar}{2\pi eH} - \frac{1}{2}\right) \pm \frac{\pi}{4}\right). \tag{2.16}$$

Several important things have to be noted. First of all, A is an extremal cross sectional area of all possible cuts through the Fermi surface perpendicular to the applied magnetic field H. The contributions of all other cross sections interfere destructively. Secondly the total signal is a sum over all harmonics p of a fundamental oscillation in inverse magnetic field $1/H$. The frequencies F of quantum oscillations are therefore quoted in units of Tesla. Furthermore there is a direct proportionality between F and the area A that depends only on universal constants. By measuring the effect of these oscillations in the density of states on the entropy of the system (magnetothermal oscillations) or the resistivity (Shubnikov–de Haas effect) one can, therefore, obtain information about the size of the extremal areas of a Fermi surface. In particular if the Fermi surface is quasi-two-dimensional (i.e. a tube) the cross section and thereby the oscillation frequency should be proportional to $1/\cos(\Theta)$ with Θ being the angle between the applied magnetic field and the principal axis of the Fermi surface.

If the effect is observed in the longitudinal magnetisation $M_{||}$ or AC magnetic susceptibility it is usually referred to as the de Haas–van Alphen effect. $M_{||}$ can be shown to be proportional to

$$\tilde{M}_{||} \propto \left(\frac{eH}{c\hbar}\right)^{3/2} \frac{m^*}{H} \sum_{p=1}^{\infty} \frac{1}{p^{1/2}} \sin\left(2\pi p\left(\frac{Ac\hbar}{2\pi eH} - \frac{1}{2}\right) \pm \frac{\pi}{4}\right) \tag{2.17}$$

and therefore contains equivalent information on the quantum oscillation frequencies and thereby on extremal Fermi surface orbits.

2.1.2.3 Effect of Temperature on Oscillations

At non-zero temperature the occupation of energy levels does not have a sharp discontinuity at ϵ_F but varies smoothly according to the Fermi-Dirac distribution $f(\epsilon, \mu)$ with μ being the chemical potential. Pippard [12] proposed a simple argument for the effect of temperature on quantum oscillations. He assumed that one can view the smooth Fermi–Dirac distribution as a superposition of a range of systems at zero temperature with slightly different chemical potentials. The overall measured oscillations can therefore be thought of as the phase coherent sum over all these systems. Mathematically, this is equivalent to a convolution of the zero temperature oscillations with the distribution function given by the derivative of the Fermi–Dirac distribution, i.e. $-\mathrm{d}f(\epsilon, \mu)/\mathrm{d}\epsilon$. It can be shown that this effectively leads in frequency space to a multiplication of the amplitude of the frequency spectrum with a temperature and field dependent prefactor R_{LK} given by

$$R_{LK} = \frac{x}{\sinh(x)},$$

where

$$x = 2\pi^2 kTm^* c/e\hbar H. \tag{2.18}$$

This is called the Lifshitz–Kosevich (LK) temperature dependence of quantum oscillations. Since the functional form depends on the effective mass m^* one can extract this information from the measured temperature dependence of each of the observed frequencies in the spectrum. Quantum oscillations can therefore be used as a Fermi surface specific probe of the effective mass.

Effect of Impurities

At the end of this section a comment should be made on the impurity dependence of the oscillation amplitude. A crucial component of the theory is the quantisation condition due to closed orbits in momentum space. The presence of impurities means that an orbiting electron will be scattered at a rate τ that is related to the

mean free path l of the sample via the Fermi velocity $\mathbf{v}_F = l/\tau$. This is equivalent to a finite lifetime of the Landau levels and results in a phase smearing of the oscillations. It can be shown that the amplitude of oscillations due to this effect depends exponentially on the mean free path l and the magnetic field H. Quantum oscillations are therefore usually only seen in very pure single crystals and/or high magnetic fields. in particular since the dependence on mean free path l is exponential even small improvements in sample quality can significantly improve the signal.

2.1.3 Electric Transport

Empirically it is found that the low temperature resistivity ρ as a function of temperature T for most metals is described by

$$\rho = \rho_0 + AT^2, \tag{2.19}$$

with ρ_0 being a temperature independent constant and A a material specific prefactor. From the semiclassical equations it would follow that the momentum $\mathbf{k}$ of an electron wavepacket is related to an applied electric field $\mathbf{E}$ via

$$\hbar\dot{\mathbf{k}} = -e\mathbf{E}. \tag{2.20}$$

This would imply that the momentum of the electron would grow in time without bounds, implying infinite conductivity. Therefore, in the absence of any inelastic scattering processes, the resistivity would be zero. One obvious source for such processes is impurity scattering, which cause the temperature independent contribution ρ_0 of the resistivity. Since electron–electron scattering cannot take place in the non-interacting electron approximation the only other possibilities for inelastic scattering are electron–phonon processes. These indeed give a temperature dependent contribution, however it is found to generally be proportional to T^5 at low temperatures and not the dominant source of scattering in materials with strong electron–electron interactions. It is one of the failures of the non-interacting electron approximation not to be able to explain the T^2 dependence of the resistivity, since it is dominated by electron–electron processes that are explicitly excluded. I will return to this problem briefly in the context of Fermi liquid theory.

Before finishing this section a brief comment on the magnetoresistance in high magnetic fields should be given.[2] It follows from an analysis of the semiclassical model of a single Fermi surface[3] that, if one applies a magnetic field $\mathbf{H}$ perpendicular to an electric field $\mathbf{E}$, the induced current $\mathbf{j}$ is related to $\mathbf{E}$ via

[2] The high field limit here is the same as for quantum oscillations.

[3] The presented equations only hold for closed Fermi surfaces. Open orbit surfaces require a separate treatment discussed for example in [6].

$$\mathbf{E} = \boldsymbol{\rho}_N \mathbf{j}, \tag{2.21}$$

with $\boldsymbol{\rho}_N$ being the resistivity tensor of the Nth Fermi surface. ρ_N has the form

$$\boldsymbol{\rho}_N = \begin{pmatrix} \rho & -RH & 0 \\ RH & \rho & 0 \\ 0 & 0 & 0 \end{pmatrix} \tag{2.22}$$

if the magnetic field is applied the z-axis and the electric field along the x-axis. Here R is the Hall coefficient and ρ is the high field limit of the longitudinal resistivity. It can be shown that ρ saturates in this limit and becomes independent of magnetic field [6]. In a material with N Fermi surfaces each of them can be thought of as a separate conductance channel. Therefore, their resistance tensors $\boldsymbol{\rho}_n$ are added in parallel resulting in an overall resistance of the form

$$\boldsymbol{\rho} = \left(\sum_{n=1}^{N} \boldsymbol{\rho}_n^{-1} \right)^{-1}. \tag{2.23}$$

2.1.4 The Fermi Liquid

All results presented in the previous sections were based on the gross simplification of neglecting electron–electron interactions. Nevertheless, they are found to agree with most of the experimentally observed behaviour of a wide range of metals. In this section a theory of the interacting Fermi liquid will be introduced that was originally developed by Landau in a series of papers [1, 2, 3]. It not only shows how the previous results are stable even with strong electron–electron interactions but also gives insight into some of the previously unresolved issues such as the temperature dependence of resistivity. As the name suggests, Landau's Fermi liquid theory describes the properties of a system of Fermions that are strongly interacting not dissimilar to the strong interactions of atoms in a liquid.[4]

The first important component of Landau's theory is what is now known as the adiabatic continuity principle. Here one assumes that the interactions are 'switched on' from zero and increased continuously to their final magnitude. In this way the eigenstates of the non-interacting problem will evolve in a continuous way to the eigenstates of the fully interacting problem. Therefore, there exists a one-to-one correspondence between the low-lying excitations of the non-interacting and the interacting system. Due to this correspondence it is possible to still label the interacting quantum states with the quantum numbers of the non-interacting eigenstates, keeping in particular the distinction between occupied and unoccupied

[4] Though I will discuss here the theory primarily in terms of electrons it should be pointed out that it applies to all interacting Fermion systems, such as, for example, liquid ^{3}He.

levels. This preserves the concept of the Fermi energy ϵ_F and the Fermi surface. However, even though the elementary excitations which empty an occupied level and fill an unoccupied one obey Fermi statistics, they are no longer single electron excitations but excitation of the whole Fermi liquid. These excitations are therefore often called quasiparticles. An important difference to single particle excitations is that quasiparticle excitations are not independent of each other. An elementary excitation of the Fermi liquid involves a redistribution of the charge density which is the source of a residual interaction between the quasiparticles. This causes the life time of quasiparticles to be finite. It is therefore not a priori clear that they constitute a good description of the system on the timescale of an experiment.

The second important component of Landau's Fermi liquid theory addresses this issue by analysing the lifetime of quasiparticles due to interactions. The main effect limiting the lifetime of a high-energy quasiparticle excitation of energy ϵ is the decay into excitations of lower energy under conservation of the symmetry in the number of particles and holes. It can be shown that the decay rate for a single excitation in the presence of an otherwise filled Fermi sea is proportional to $(\epsilon - \epsilon_F)^2$. Based on this it can be argued that there can always be found a temperature T below which the excitations are sufficiently long lived such that on the time scale of the experiment the quasiparticle picture is an appropriate description of the system. This phase space protection of the scattering rate between quasiparticles is also the origin for the T^2-term in the temperature dependence of the resistivity.

In summary, these two fundamental concepts of the theory show that at sufficiently low temperature the excitations of a Fermi liquid take the form of quasiparticles that obey Pauli's exclusion principle. Furthermore, the concepts of filled and empty states, and therefore of a Fermi surface are preserved. An important consequence is that any property whose derivation in the non-interacting picture only takes into account properties close to the Fermi surface should still hold in the framework of Fermi liquid theory.

What does change contrary to the non-interacting case is therefore not the functional form of most of the physical properties of the system but the absolute values and the range of external parameters, such as temperature, over which it is applicable. This explains why the theory of a Fermi gas is so successful in qualitatively describing properties of a wide range of crystalline solid state systems at low temperatures without taking full account of electron–electron interactions.

The enhancement of the properties of the system with respect to the non-interacting band structure values is phenomenologically described by so-called Landau Fermi liquid parameters. These encapsulate the effect of interactions on the observable quantities in a phenomenological way. They represent, in principle, the prefactors of an expansion of the momentum and spin dependent interaction energy in harmonics of the Fermi surface. For the case of a spherical Fermi surface this can be done explicitly as an expansion in spherical harmonics. Here one finds for the measured effective mass m^* an enhancement over the non-interacting band mass m_{band} given by

$$m^* = \left(1 + \frac{F_1^s}{3}\right) m_{band}. \tag{2.24}$$

Furthermore the magnetic susceptibility is enhanced as

$$\chi = \frac{m^*}{m_{band}} \frac{1}{1 + F_0^a} \chi_{band}, \tag{2.25}$$

with F_1^s and F_0^a being two Landau parameters for an isotropic Fermi surface such as, for example, in the case of liquid ^{3}He at low temperatures. The factor $1/(1 + F_0^a)$ is also often referred to as the Sommerfeld–Wilson ratio of a Fermi liquid. It describes the ratio between the spin susceptibility and the effective mass enhancement and can therefore be thought as a guide to the importance of magnetic quasiparticle interactions.

An interesting observation relating to the prefactor A of the temperature dependent part of the resistivity was made by Kadowaki and Woods [13]. When plotting for a range of materials A versus the square of the Sommerfeld coefficient γ^2 it was found that there is a positive linear correlation between them. The ratio A/γ^2 of a material is referred to as the Kadowaki–Woods ratio. It can indeed be theoretically justified that A is proportional to the square of the effective mass $(m^*)^2$ and therefore γ^2 for a single spherical Fermi surface (see [14] and references therein). However, when considering multiband materials where the different Fermi surfaces act as parallel conductance channels but contribute 'in series' to the specific heat, it becomes apparent that the Kadowaki–Woods ratio cannot hold as a general law when considering the overall material properties but at most for the specific contribution of a single part of the Fermi surface to the overall measurable quantities.

Last but not least, it should be remarked that the electron–electron interaction and therefore the renormalisation of the electronic properties in a real multi band material are often significantly different from band to band and can even vary within a band. This again only affects the quantitative aspect of the renormalisation but does not change the qualitative functional form of those properties, as long as the basic assumptions of Fermi liquid theory such as the adiabatic continuity are not violated.

2.1.5 Beyond the Fermi Liquid

In the previous section Landau's Fermi liquid theory was introduced. Its main implication was that the functional form of the theoretical predictions of the Fermi gas also hold for strongly interacting systems at low temperatures and small excitation energies. Just how robust Landau's Fermi liquid theory is can for example be seen in heavy Fermion systems, where the charge carriers have effective masses of the order of 100 electron masses. The seemingly wide range of

applicability the success of Landau's Fermi liquid theory makes the materials in which it fails to describe particularly interesting, not in the least, to say it in Landau's own words (used in a different context), since '*especially [as] the brevity of life does not allow us the luxury of spending time on problems which will lead to no new results*' [15].

There are of course ample examples of non-Fermi liquid behaviour such as BCS superconductivity. Here, the fundamental excitations are not quasiparticles but Cooper pairs. In particular, the Kohn–Luttinger theorem [16] shows that any Fermi liquid at low enough temperatures will become superconducting. However, the theorem does not give a lower bound for that transition temperature and indeed for a number of metals no superconductivity has been observed to date.

From the scientific point of view the materials which attract particular interest are those that exhibit novel properties that do not readily agree with Landau's Fermi liquid theory or BCS superconductivity. Most notably falling into both these categories are the high temperature cuprate superconductors discovered in 1986 [4]. First these materials have an unusual superconducting state at low temperatures. Secondly the 'normal' metallic state above the superconducting transition has many characteristics that are not in agreement with a normal Fermi liquid description. However it should be noted here that this does not exclude the existence of quasiparticles in these materials. In particular, for special representatives of these compounds in which the normally present disorder due to carrier doping is suppressed, it was possible to observe the above described phenomenon of quantum oscillations [17, 18, 19]. There is an exciting range of other materials and concepts that show non-Fermi liquid physics such as the fractional quantum Hall effect systems [20] and Kondo lattice systems [21].

Particular interest in recent years has been caused by systems that can be tuned by an external parameter from Fermi liquid behaviour to non-Fermi liquid behaviour due to their closeness to a so-called quantum critical point. In the following I will introduce both from an experimental and theoretical point of view the concept of quantum criticality and its implications. This can be by no means exhaustive due to the large amount of research existing in the field and the mathematical complexity involved in the theory. More detailed accounts are given in several extensive reviews covering both experimental and theoretical aspects [21, 22, 23].

2.1.5.1 Quantum Criticality

Second order phase transitions at finite temperature usually occur between a high temperature disordered and a low temperature ordered phase. The order is characterised by an order parameter that starts to grow continuously in the ordered phase from zero at the transition temperature. A typical example is the transition from a paramagnetic to ferromagnetic phase with the order parameter being the magnetisation M. An important aspect of second order transitions is that coherent fluctuations in the order parameter diverge both in length and timescales on

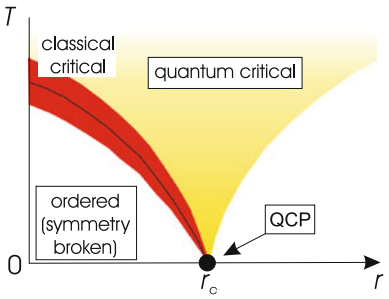

Fig. 2.4 The figure shows a generic scenario of quantum criticality. For details see text

approaching the transition temperature from either side. In particular, the diverging time scale implies that the associated characteristic frequency ω and thereby the energy scale $\hbar\omega$ of these fluctuations goes towards zero. However, as soon as this energy scale is much smaller than that given by the temperature T, i.e. $\hbar\omega \ll k_B T$ they are effectively classical in nature. For classical fluctuations only the spatial dimensions have to be taken into account. Therefore, the critical fluctuations of any finite temperature second order phase transition fall into the universality classes of classical second order phase transitions.

However, if one can suppress the finite temperature transition towards $T = 0$ by using a tuning parameter such as pressure or magnetic field, then the region over which the critical fluctuations are classical in nature also shrinks to zero. This situation is shown schematically in Fig. 2.4. Here the second order transition line between the disordered and ordered state is shown in black with the region of classical fluctuations around the transition being indicated in red. When suppressing the second order phase transition towards zero temperature then the region over which the classical critical fluctuations dominate is reducing. If one crosses the transition at $T = 0$ as a function of the control parameter r then the critical fluctuations associated with the phase transition at r_C have a purely quantum mechanical nature, hence the name quantum critical point. It is here where the description of Fermi liquid theory generally breaks down.

Above r_C one generally observes a finite temperature cross-over towards a Fermi liquid like behaviour at low temperatures. The quantum critical behaviour is expected to become non-universal above sufficiently high temperatures.

This kind of physics has been especially well studied in heavy Fermion compounds, where often occurring ferromagnetically or antiferromagnetically ordered ground states can potentially be suppressed in temperature by the application of magnetic field or pressure.

Two examples are shown in Fig. 2.5. On the left hand side the phase diagram of $YbRh_2Si_2$ is shown in the $H - T$ plane ([25], graphic reproduced from [23]). Here the colour scheme shows the power law of the temperature dependence of the resistivity, with blue being 2 (Fermi liquid like behaviour) and the other end of the colour scale (orange) corresponding to 1. On applying a magnetic field one observes a suppression of the antiferromagnetic phase to below the experimentally accessible range. At the critical field the temperature dependence of the resistivity

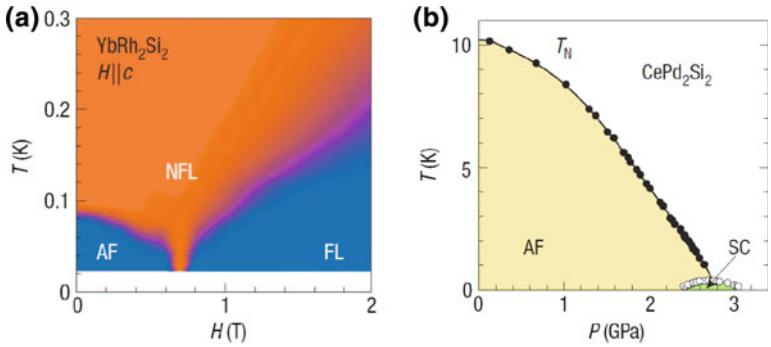

Fig. 2.5 Two examples of materials believed to be close to a quantum critical point (graphics reproduced from [23]). **a** The exponent of the temperature dependent part of resistivity for $YbRh_2Si_2$ as a function of temperature T and magnetic field H as derived from the logarithmic derivative of the resistivity with respect to temperature [25]. The colour scheme runs from 1 (*red*) to 2 (*blue*). The low field/low temperature phase is antiferromagnetic whereas the high field/low temperature phase is consistent with Fermi liquid like behaviour. In between the two states a quantum phase transition is expected to occur at the field where the measured resistivity is linear down to lowest temperatures. **b** The phase diagram of $CePd_2Si_2$ as a function of pressure. Again an antiferromagnetic phase transition is suppressed towards $T = 0$. However, at low temperatures a superconducting phase intervenes. The superconductivity is believed to be unconventional in that it is mediated by magnons rather than phonons

is non-Fermi liquid like over the whole range. At higher fields Fermi liquid behaviour in the resistivity is recovered.

In Fig. 2.5b the phase diagram of $CePd_2Si_2$ under pressure is shown [26] (Graphic reproduced from [23]). Here again the second order phase transition is suppressed towards zero temperature, this time by applying pressure.

In the second example a particularly significant aspect of quantum criticality is realised. What is often observed in the vicinity of quantum critical points is the stabilisation of novel phases with physical properties not usually observed. In $CePd_2Si_2$ for example the superconducting ground state is believed not to be due to electron–phonon interactions but to electron–magnon interactions [26]. This is particularly surprising since conventional superconducting states are destroyed by magnetic interactions.

The currently most successful approach in describing the quantum critical phenomenon was pioneered by Hertz [27] and Millis [28]. This theory is based on a renormalisation group approach similar to the theory of classical critical phenomena and leads to a classification of quantum phase transitions into certain universality classes. The fundamental difference is that for quantum phase transitions it is not only spatial but also temporal fluctuations that are included in the quantum mechanical action describing the system. Discussing Hertz–Millis theory in detail is beyond the scope of this brief introduction to the subject. However good introductions can be found in the aforementioned review articles [21, 22, 23]. Some of the results thought to apply to $Sr_3Ru_2O_7$, the system studied in this project, will be summarised in Sect. 2.2.2.

2.2 The Physics of the Ruthenate Family

Having discussed the general aspects of the physics of metals, this section will concentrate on the relevant experimental data and theoretical models specific to $Sr_3Ru_2O_7$, the material studied in this project, and Sr_2RuO_4, whose physical properties are of importance for the characterisation of the experimental setup developed for the measurements.

Both materials have generated significant scientific interest. Sr_2RuO_4 was the first layered perovskite material isostructural to the high-T_C cuprates that was found to be superconducting [29]. The transition temperature of 1.5 K is rather low compared to the high-T_C's, but it was proposed early on [30] to be one of a few superconducting materials whose order parameter has p-wave symmetry. A detailed presentation of the physics of Sr_2RuO_4 can be found for example in the review article by Mackenzie and Maeno [31].

$Sr_3Ru_2O_7$ is on the other hand in its zero-field ground state a highly enhanced paramagnet with a Wilson ration of ≈10 [32]. For comparison, the Wilson ratio of ^{3}He is 4 (see for example [33]). The interest in the material grew dramatically when the magnetic field phase diagram was studied in detail in a series of papers [34, 35, 36], reporting not only signatures consistent with a quantum critical point but also the existence of a novel phase in its vicinity that shows evidence of 'electron-nematic' properties in transport measurements.

2.2.1 Crystal Structure and Synthesis

The materials discussed in this thesis belong to the Ruddlesden–Popper strontium ruthenate series with the chemical formula $Sr_{n+1}Ru_nO_{3n+1}$, of which Sr_2RuO_4 and $Sr_3Ru_2O_7$ are the $n = 1$ and $n = 2$ members respectively. Their ideal crystal structures are shown in Fig. 2.6.

The fundamental building blocks are layers of corner-sharing ruthenium oxide octahedra. The number of adjacent RuO_2 layers is the reason for calling the materials the single-layer and bi-layer members of the series respectively. In between layers, Sr cations are arranged as shown.

The crystal structure of Sr_2RuO_4 with the tetragonal space group $I4/mmm$ is faithful to the above ideal representation. The lattice parameters are $a = b = 3.862$ Å and $c = 12.722$ Å [38]. Contrary to that, the octahedra in $Sr_3Ru_2O_7$ show a small counter rotation of the octahedra by 7° [39]. The rotation direction alternates between the planes within a bi-layer. This structural difference causes a $\sqrt{2} \times \sqrt{2}$ reconstruction of the unit cell in the ab-plane and changes the space group of the material to the orthorhombic $Bbcb$ with $a \approx b = 5.5$Å [39, 40]. This has significant implications for the electronic structure as will be shown further on.

The first single crystal samples of $Sr_3Ru_2O_7$ were grown by Cao et al. [41] with the flux-growth method. These samples were found to be ferromagnetic

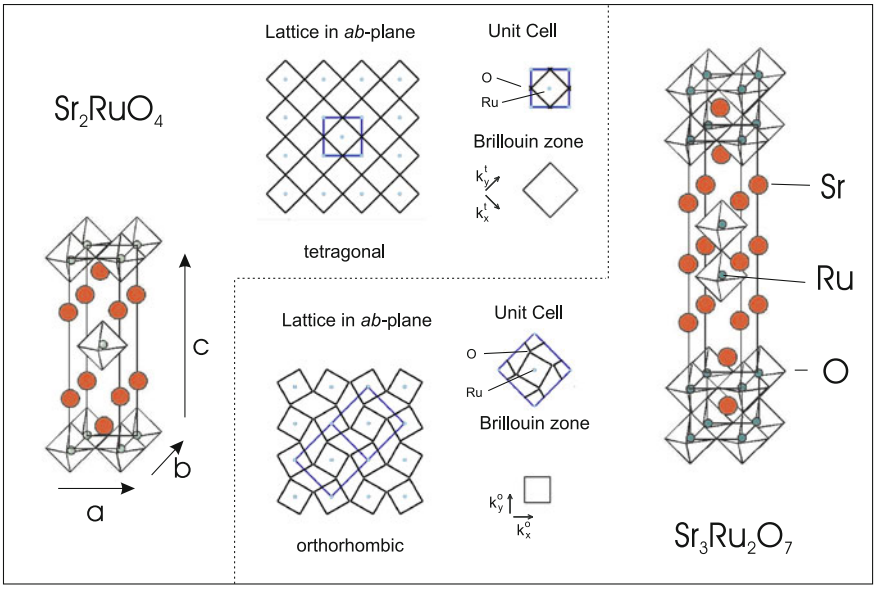

Fig. 2.6 Here the crystal structure is summarised for Sr_2RuO_4 and $Sr_3Ru_2O_7$ (graphics partially reproduced from [37]). Please see text for details

below 100 K. The material was subsequently synthesized in single crystal form by Ikeda et al. [42] by employing infra-red image furnace growth and found to be paramagnetic at low temperatures. The previously observed ferromagnetism was most probably due to inclusions of $Sr_4Ru_3O_{10}$ impurities. Since the image furnace grown crystal have a significantly improved quality they are referred to as second generation samples in the following. The thermodynamic properties, especially in magnetic field, were found to depend significantly on the sample quality and after a detailed growth study by Perry et al. [43] it was possible to reduce the residual resistivity of the materials by an order of magnitude (third generation samples). As will be seen in the following sections one cannot underestimate the importance of working with the highest purity samples available.

2.2.2 Thermodynamic Properties and Magnetic Phase Diagram

In the following I will introduce the phase diagram and the associated properties of the materials as established by previous measurements. I will in particular concentrate on thermodynamic measurements as well as resistivity before discussing the microscopic electronic structure in more detail in the next section.

2.2.2.1 $Sr_3Ru_2O_7$

Zero Field Low Temperature Properties

The crystal structure of $Sr_3Ru_2O_7$ is highly anisotropic, and this anisotropy is reflected in a number of properties such as its resistivity. In Fig. 2.7 the in-plane resistivity ρ_{ab} as well as the resistivity along the c-axis, ρ_c, are shown as a function of temperature T for second generation samples [32]. A pronounced asymmetry not only exists in the residual resistivity at zero temperature (observe the different scales for ρ_{ab} and ρ_c), but also in the A coefficient of the T^2 behaviour, as can be deduced from the gradient of the curves in the inset where the low temperature resistance is plotted against T^2.

The electronic specific heat c_{el} divided by temperature T is reproduced in Fig. 2.8a from [44] (data points not relating to the zero field properties have been

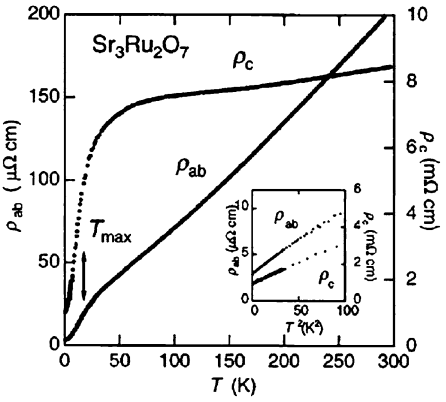

Fig. 2.7 In-plane and c-axis resistivity ρ_{ab} and ρ_c of $Sr_3Ru_2O_7$ as a function of temperature [32] (note the different scales for ρ_{ab} and ρ_c). The *inset* shows the same data in the low temperature range as a function of T^2

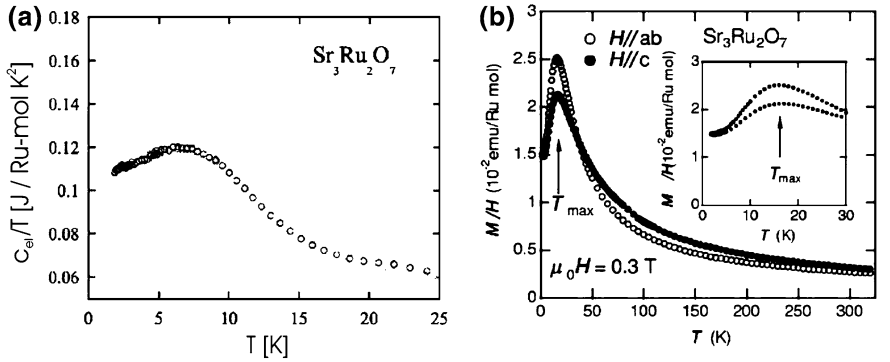

Fig. 2.8 **a** The electronic specific heat c_{el} of $Sr_3Ru_2O_7$ divided by temperature T as a function of T [44]. **b** The low field DC magnetic susceptibility of $Sr_3Ru_2O_7$ as a function of temperature T for the magnetic field applied along the crystallographic c-axis (*full circles*) and in the *ab*-plane (*open circles*) [32]. The *inset* shows a magnification of the low temperature range of the data

removed for clarity). c_{el}/T has a finite zero-temperature value corresponding to a Sommerfeld coefficient γ of 110 mJ/Ru-mol K^2, which is relatively large in the context of the ruthenates. Furthermore, there is a significant hump in the specific heat at a temperature of the order of 8 K that is in general associated with the metamagnetic feature discussed later on.

As mentioned before, $Sr_3Ru_2O_7$ is found in zero field to be a highly enhanced paramagnet. Figure 2.8b shows the DC magnetic susceptibility as determined by measuring the magnetisation M resulting from a small applied magnetic field H as a function of temperature T for two different orientations of H [32]. Here one can see a remarkably isotropic susceptibility at low temperatures even though the material itself is strongly anisotropic, suggesting that the Pauli term dominates the paramagnetism (see Sect. 2.1.2). From the above measurements a Wilson ration of $\approx$10 can be deduced.

Metamagnetism and Quantum Criticality

The unusually high Wilson ratio can be interpreted as $Sr_3Ru_2O_7$ being a paramagnet close to a magnetically ordered state. Indeed when applying a magnetic field one can observe a rapid superlinear rise in magnetisation at a well defined field. This phenomenological effect is called metamagnetism and is commonly encountered in local moment systems [45] undergoing spin-flip or spin-flop transitions. Figure 2.9a shows the magnetisation of $Sr_3Ru_2O_7$ as a function of applied magnetic field for several temperatures [44]. Here the field is applied in the crystallographic *ab*-plane. The metamagnetic feature at approximately $5T$ is clearly identifiable and is more defined towards lower temperatures.

Grigera et al. [46] studied the AC magnetic susceptibility systematically as a function of temperature as well as magnitude and direction of the applied magnetic field. They found that with the field applied in the *ab*-plane the metamagnetic cross-over turns into a first order phase transition as indicated by a dissipative out of phase component of the AC susceptibility. This first order transition line terminates in a critical end point at approximately 1.2 K. What caused particular interest was that the temperature of the critical end point could be suppressed as a function of angle of the applied magnetic field, leading to the possibility of a new class of quantum critical point—a so-called quantum critical end point [34]. The state of the phase diagram in second generation samples is summarised in Fig. 2.9b. Here, the position of the resulting sheet of first order transitions as a function of magnetic field, field direction and temperature is shown in green. The black line indicates the experimentally determined position of critical end points. The critical field moves towards higher values as the field is rotated towards the *c*-axis. At $B||c$ the critical endpoint is suppressed to below experimentally measurable temperatures. This particular orientation of magnetic field is the main focus of the project reported in this thesis.

The most precise early evidence for quantum criticality in this system was obtained by a detailed study of magnetotransport. The resistivity data were

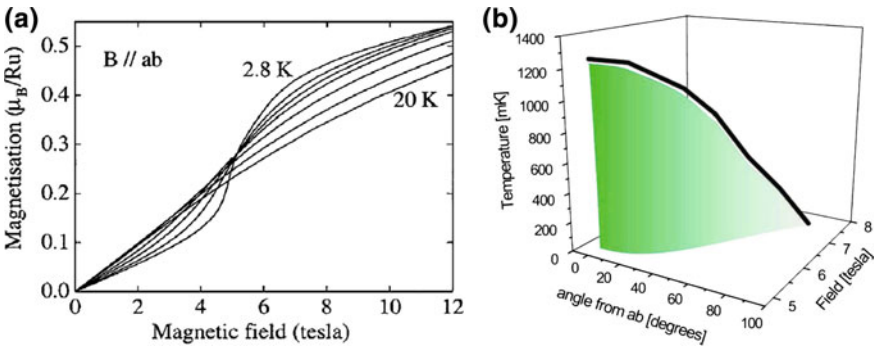

Fig. 2.9 **a** The magnetisation of $Sr_3Ru_2O_7$ as a function of applied magnetic field for a range of temperatures between 2.8 and 20 K [44]. The field is applied in the crystallographic *ab*-plane. The superlinear rise at low temperatures is the metamagnetic feature discussed in the text. **b** The *green* surface denotes the position of the metamagnetic first order transitions observed in second generation samples of $Sr_3Ru_2O_7$ as a function of field magnitude, field orientation (as angle between the magnetic field and the *ab*-plane) and temperature T [46]. The sheet of first order transitions terminates in a line of critical end points shown in *black*. For the field applied along the *c*-axis (90° on the angular scale) the data are consistent with the critical end point being suppressed to zero temperature

analysed at several magnetic fields H under the assumption that ρ is a combination of a temperature independent impurity scattering term, the residual resistivity ρ_{res}, and a temperature dependent power law contribution AT^{α}, i.e.

$$\rho(T,H) = \rho_{res}(H) + A(H)T^{\alpha}. \tag{2.26}$$

In a Fermi liquid scenario α would be 2. Quantum critical theories however predict different power laws for the temperature dependence according to the universality class of the particular transition observed. A study by Millis et al. [47] analysed $Sr_3Ru_2O_7$ in particular and found that the temperature exponent should be 1 at the critical field H_C.

The main results of the experimental study are shown in Fig. 2.10 [34]. In panel (a) the extracted temperature exponent as a function of magnetic field[5] is shown. On approaching the critical field, the range in temperature over which the exponent of 2 consistent with Fermi liquid behaviour is observable, shrinks to below the lowest measured temperature. At the critical field a close to linear temperature behaviour is observed whereas at higher magnetic fields Fermi liquid like behaviour is recovered.

In panel (b) both the extracted residual resistivity ρ_{res} as well as the A coefficients extracted at lowest temperatures are plotted as a function of field in the vicinity of the critical field at $H_C \approx 8\,\mathrm{T}$. The increased A coefficient in the vicinity

[5] To be more precise it is the logarithmic derivative of the temperature dependent part of the resistivity ρ with respect to temperature T, $\partial \ln(\rho - \rho_0)/\partial \ln T$, that is shown. Here ρ_0 is the residual resistivity. For more details see [34].

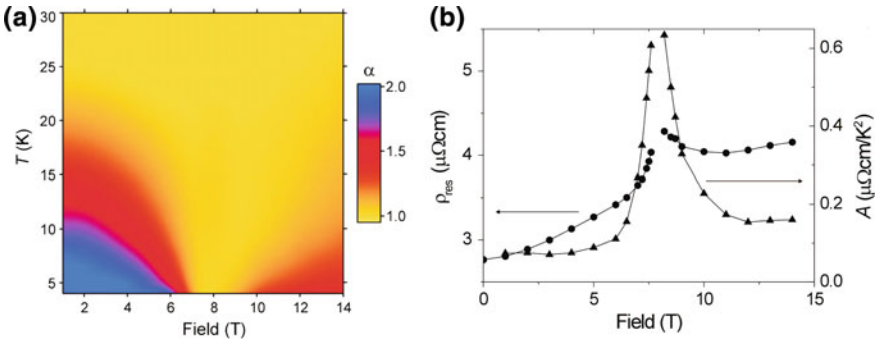

Fig. 2.10 **a** The logarithmic derivative of the temperature dependent part of the resistivity with respect to temperature as a colour scale in the magnetic field and temperature plane [34]. In the case of a pure power law AT^{α} this is equal to α. **b** The residual resistivity ρ_0 as well as the coefficient A of the temperature dependent part of the resistivity as a function of magnetic field and temperature (note the different scales of ρ_0 and A). For details of the parameter extraction from the original data please refer to [34]

of H_C indicates, in conjunction with the Kadowaki–Woods ratio (see Sect. 2.1.4), an increase in the effective quasiparticle mass of at least a fraction of the Fermi liquid excitations. However, a detailed theoretical understanding of this ratio in a realistic multiband system in a magnetic field is not developed completely. Therefore, a thermodynamic study of the specific heat is necessary to address the issue, in particular since the quantum critical scenario makes specific predictions about the temperature and field dependence of the specific heat [47, 48]. Furthermore the peak of residual resistivity at the critical field seems to suggest that the increase of the quasiparticle mass is accompanied by an increase of the impurity scattering. In hindsight this feature is most probably associated with the phase formation observed in the high purity third generation samples as discussed below.

Experimental evidence consistent with a quantum critical scenario was observed in the measurement of the electronic specific heat c_{el} close to the critical field at temperatures above 1.5 K by Perry et al. [44]. The results are shown in Fig. 2.11. Here c_{el} divided by temperature T is shown as a function of T for a range of magnetic fields. The field direction is parallel to the crystallographic c-axis. In particular, the functional form of the data at 7.7 T was found to be consistent with c_{el}/T having a singular component that diverges logarithmically at $T = 0$ consistent with a quantum critical scenario [47].

Novel Quantum Phase and Nematic-Like Transport

The possibility of studying quantum criticality in a clean system motivated a detailed study into the optimisation of the crystal growth parameters by Perry et al. [43]. In the resulting third generation samples, mean free paths of the order of

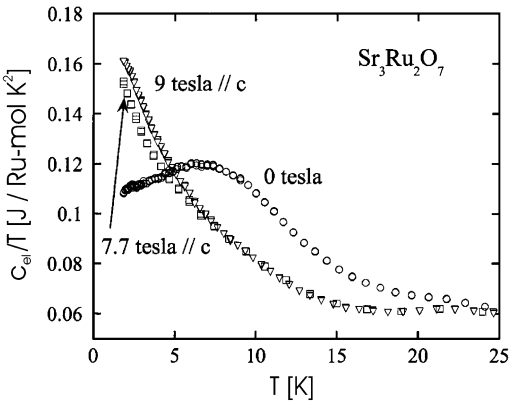

Fig. 2.11 Electronic specific heat c_{el} divided by temperature T as a function of T. Measurements have been done in zero field, 7.7 T and 9 T with the field oriented parallel to the crystallographic c-axis [44]

3,000 Å were observed. In these samples it was found by Grigera et al. [35] that in the vicinity of the proposed quantum critical end point a novel phase is stabilised which consequently is strongly disorder sensitive.

Figure 2.12 presents the experimental evidence for this phase as seen in electric transport and several thermodynamic measurements [35]. Part (a) shows the resistivity as a function of field for several temperatures. The resistance curves describe a distinct region as a function of magnetic field between 7.8 T and 8.1 T in which the resistivity is significantly increased and a much weaker temperature dependence observed compared to the surrounding states.

Experimental evidence that these features indeed mark first order phase transitions is shown in part (b). Here both the in-phase and out of phase components of the AC magnetic susceptibility[6] χ' and χ'' as well as the linear magnetostriction λ are shown as a function of magnetic field H for a sample temperature of 100 mK. The features (1) and (2) coincide with the boundaries of the anomalous resistive region in the previous graph. Furthermore the clear signatures in the loss term χ'' indicate that these are first order transitions. The width of the transitions as seen here is 50 mT. Feature (3) is a metamagnetic cross-over that is much wider in magnetic field and does not show up in χ''. In the inset of Fig. 2.12b a trace of magnetisation M as a function of temperature T is shown at the critical field H_C. Here a clear change in temperature dependence at 1.2 K is an indication for a thermodynamic transition into the new phase. However, further definite thermodynamic proof is needed to establish its exact nature.

Finally in Fig. 2.13 the magnetisation of ultra clean $Sr_3Ru_2O_7$ as a function of applied magnetic field is shown (data provided by R.S. Perry). The field orientation is parallel to the crystallographic c-axis and the sample temperature is 70 mK. The magnetisation is raising very fast at the transitions (1) and (2) and the crossover (3). The labels here correspond to the same used in Fig. 2.12.

[6] Strictly speaking AC magnetic susceptibility is not a thermodynamic probe but frequency dependent.

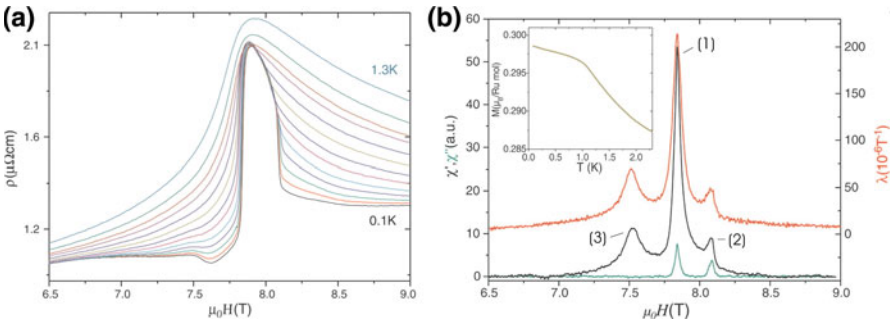

Fig. 2.12 **a** The in-plane resistivity of a third generation $Sr_3Ru_2O_7$ sample as a function of magnetic field H for several temperatures between 0.1 and 1.2 K [35]. The field is applied along the crystallographic c-axis. **b** Measurements of the components χ' and χ'' of the complex AC magnetic susceptibility as well as the linear magnetostriction λ as a function of magnetic field. Here the sample temperature is 100 mK and the field is applied along the c-axis. The *inset* shows the magnetisation of $Sr_3Ru_2O_7$ as a function of temperature at ≈8T, a field in between the two first order phase transitions that are observed in the other thermodynamic quantities [35]. Furthermore the two features coinciding with the resistive boundaries in **a** are labelled (*1*) and (*2*)

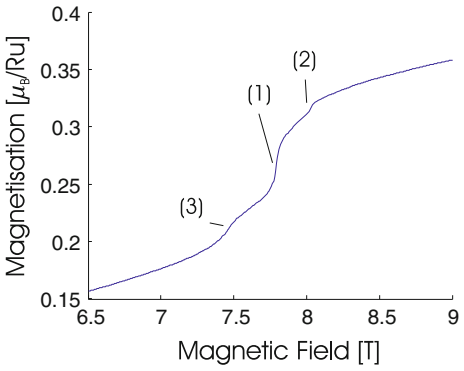

Fig. 2.13 Magnetisation of third generation $Sr_3Ru_2O_7$ samples as a function of applied magnetic field. The field orientation is parallel to the crystallographic c-axis and the sample temperature is 70 mK. The labels (*1*)–(*3*) are explained in the text (data provided by R.S. Perry)

That the novel phase between the boundaries (1) and (2) has indeed highly unusual resistive properties has been established by Borzi et al. [36] in a careful study of the resistivity as a function of not only applied field H and temperature T but also of the angle between the current I and H. In particular Fig. 2.9a shows the resistivity as a function of magnetic field H with the field applied at 77° from the crystallographic ab-plane. This field can be thought of as a linear combination of a field H_c parallel to the c-axis and a small added component H_a along the a-axis. Here, the label a has been chosen instead of b arbitrarily since a and b are interchangeable. The current I can now be applied either along ($I_{\|}$—shown in black) or perpendicular ($I_{\perp}$—shown in red) to the in plane field component H_{ab} as shown in the inset in Fig. 2.14a. While the resulting curves outside the new phase are indistinguishable, their behaviour inside the phase is dramatically different.

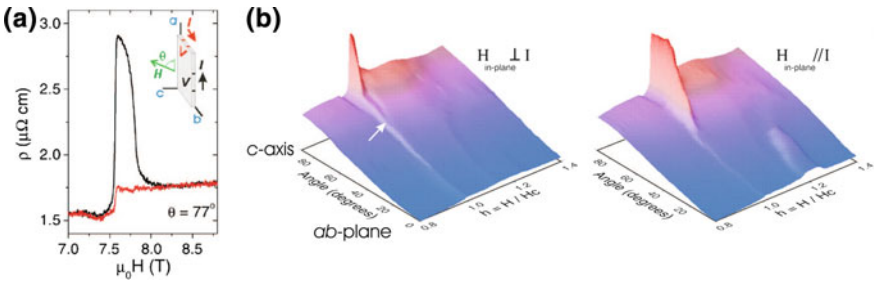

Fig. 2.14 **a** The resistivity ρ as a function of field H with the field applied at 77° from the *ab*-plane (i.e. close to the *c*-axis) [36]. The two traces correspond to the current being parallel to the in-plane component of the field (*black*) and perpendicular to it (*red*) as shown in the inset. **b** The in plane resistivity as a function of orientation and magnitude H of magnetic field. The two graphs correspond to the two different orientations of the current I with respect to the in-plane component of the magnetic field H as indicated. Please note that the field scale is given in H/H_C. Here H_C is the angle dependent position of the main first order metamagnetic transition. Furthermore, on the angular scale 90° corresponds to the magnetic field being applied parallel to the *c*-axis and 0° to the magnetic field being in the *ab*-plane. The *white arrow* indicates the point at which the two first order transitions enclosing the novel quantum phase merge, within experimental resolution

Anisotropic transport in itself is not unusual. Here, however, first of all it has been found in an accompanying neutron study that while the transport is anisotropic one cannot distinguish between the values of *a* and *b* within experimental resolution even under an applied in-plane magnetic field. Instead the data indicate that the symmetry breaking revealed by transport is intrinsic and the small applied in-plane magnetic field is merely 'aligning' different regions of domains of an intrinsically symmetry broken phase. In combination the results by Borzi et al. are consistent with the electronic liquid breaking the (discrete) rotational symmetry of the lattice—a behaviour called, in analogy to nematic phases in liquid crystals, *'electronic nematicity'*.

The full angular dependence for $I_{\parallel}$ and $I_{\perp}$ as a function of magnitude of applied field and orientation of the field relative to the *ab*-plane is shown in Fig. 2.14b. Please note that the field magnitude axis is divided by the critical field H_C which is angle dependent as has been discussed in the previous section. In addition to the anomalous phase close to the *c*-axis (at an angle of 90°) a further anomalous region can be identified in the *ab*-plane.

Finally, before ending this section, the most relevant information on the position of phase transition lines and the observance of 'electron-nematic'-like behaviour is summarised in Fig. 2.15. Panel (a) is reproduced from [49] and shows as a function of temperature, magnetic field and orientation of the field the position of the established first order transition lines in green whereas the regions under the blue domes are those in which the anomalous 'nematic' transport characteristics have been observed. In Fig. 2.15b the phase diagram in the *c*-axis as established by magnetisation M, AC magnetic susceptibility χ, linear magnetostriction λ and thermal expansion coefficient α is shown [35, 50]. The position of the first order

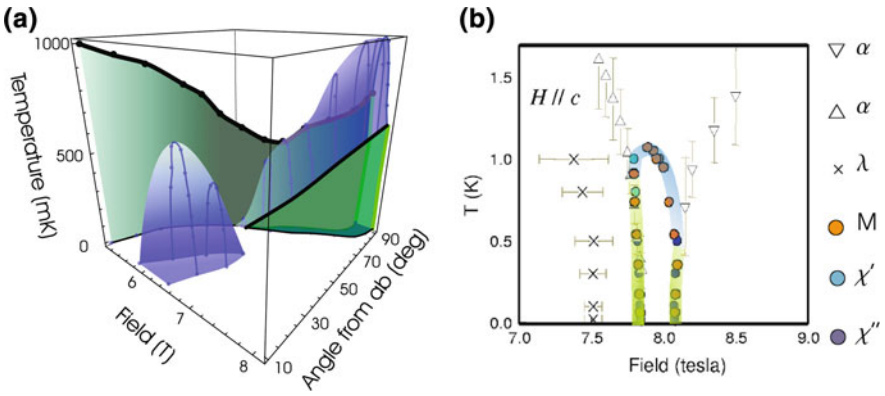

Fig. 2.15 Here the most relevant phase diagram information of high purity single crystal $Sr_3Ru_2O_7$ based on the current experimental data is shown. **a** The observed first order metamagnetic transition sheets as a function of temperature, magnetic field magnitude and orientation are shown in green. The *black lines* represent the lines of critical end points of these sheets. Furthermore the regions inside the *blue domes* have been found to show 'nematic-like' transport features as discussed in the text. On the angular scale 90° corresponds to the magnetic field being applied parallel to the *c*-axis and 0° to the magnetic field being in the *ab*-plane (figure reproduced from [49]). In **b** the phase diagram with the field applied parallel to the *c*-axis is shown. The *green lines* show the position of first order transitions whereas the blue line indicates the position of the putative second order phase transition. The other features are thermodynamic crossovers. The data points shown are extracted from DC magnetisation *M*, the components of the complex AC magnetic susceptibility χ, linear magnetostriction λ and thermal expansion coefficient α [35, 50]

transitions is marked in green as in the previous graph. The true thermodynamic nature of the 'roof' connecting the two first order transitions cannot be determined on the basis of the evidence that existed before the current project began. The other features indicated in this phase diagram are crossovers.

2.2.2.2 Sr_2RuO_4

In this section the thermodynamic properties of Sr_2RuO_4 will only be discussed insofar as they are relevant to the characterisation of the experimental setup developed in this thesis.

In zero field, Sr_2RuO_4 has a superconducting transition at $T_C = 1.5$ K. In Fig. 2.16a the electronic specific heat c_{el} divided by temperature T is shown as a function of temperature [51]. The sharp transition at T_C is clearly identifiable. Furthermore c/T above T_C is consistent with Fermi liquid theory. The magnitude of the Sommerfeld coefficient γ of the normal state is 38 mJ/Ru-mol K^2, approximately a third of the Sommerfeld coefficient observed in $Sr_3Ru_2O_7$. The results for electronic specific heat are usually quoted 'per mole ruthenium' (Ru-mol) since the valence electrons in these systems originate from the Ru 4*d*-shell as will be discussed in the next section.

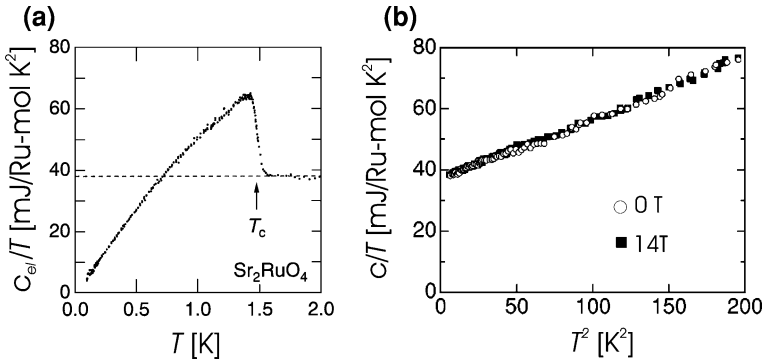

Fig. 2.16 **a** The electronic specific heat c_{el} of Sr_2RuO_4 divided by temperature T as a function of T [51]. The *dotted line* represents the normal state specific heat that would be observed if the transition to superconductivity at T_C would not take place. **b** The total specific heat c of Sr_2RuO_4 divided by temperature T as a function of T^2 with the sample being in zero magnetic field and in a field of 14T [52]

The second important feature for this project is that the specific heat of the normal state of this material is virtually independent of magnetic field. In order to illustrate this, Fig. 2.16b shows the specific heat divided by temperature as a function of T^2, for no magnetic field applied (circles) and with a magnetic field of 14 T applied (squares) [52]. The linear dependence on T^2 is caused by the phononic contribution to the specific heat.

2.2.3 Electronic Structure Properties

In the previous section the macroscopic properties of $Sr_3Ru_2O_7$ and Sr_2RuO_4 were presented. In particular it was shown that in certain regions of the phase diagram their properties are consistent with Fermi liquid theory. In this section the current experimental knowledge of the microscopic electronic structure, that is, the Fermi surface and band structure of these materials will be briefly reviewed. The section will begin with Sr_2RuO_4 since the more complicated band structure of $Sr_3Ru_2O_7$ can be understood more easily by starting from the band structure of Sr_2RuO_4.

2.2.3.1 Fermi Surface of Sr_2RuO_4

Sr_2RuO_4 is a material whose Fermi surface has been studied in great detail using quantum oscillations [54, 55]. The upper part of Fig. 2.17 shows as an example typical de Haas–van Alphen oscillations as a function of the magnetic field [53]. Due to the unusually high signal to noise ratio it is possible to observe the fundamental frequencies as well as higher harmonics as is shown in the frequency

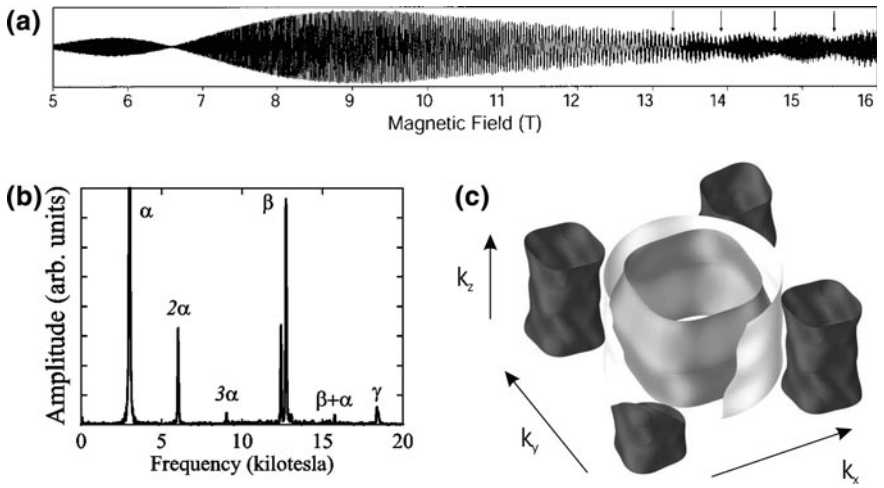

Fig. 2.17 **a** A typical trace of Sr_2RuO_4 quantum oscillations as a function of magnetic field observed in the de Haas–van Alphen effect [53]. **b** The frequency spectrum of quantum oscillation in inverse magnetic field for Sr_2RuO_4 [52]. The magnetic field is applied along the crystallographic *c*-axis. The fundamentals α, β and γ are labelled together with their harmonics and sum frequencies. **c** The Fermi surface of Sr_2RuO_4 as reconstructed from quantum oscillations in combination with LDA calculations [31]. The central surface is the β sheet surrounded by the γ surface. The α surface is centred on the corner of the Brillouin zone and shown four times here. The Fermi surface dispersions along k_z have been amplified by a factor 15 for reasons of presentation

spectrum in Fig. 2.17. In a detailed angular dependence study, Bergemann et al. [55] were able to reconstruct the Fermi surface of Sr_2RuO_4 as shown in Fig. 2.17c. It consists of three quasi-two-dimensional parts, the α, β and γ surfaces, that are relatively weakly warped in the k_z direction. The quasi-two-dimensionality can be readily understood by taking the crystal structure into account. The electronic states at the Fermi surface are derived from Ru 4*d* orbitals. Since these are arranged in layers of RuO octahedra, the hopping integral in a tight binding approach for electronic states close to the Fermi energy is significantly larger within a plane than in between planes. This leads to a very weak dispersion of the energy bands in the k_z direction of momentum space resulting in the observed quasi-two-dimensionality of the Fermi surface.

The quantum oscillation findings have been largely confirmed by ARPES measurements [56] and LDA band structure calculations [57], as shown in Fig. 2.18a and b, respectively.

ARPES and quantum oscillation measurements in $Sr_{2-x}La_xRuO_4$ samples, which are effectively electron-doped, made a definite identification of the α sheet as being of 'hole'-like character and the β and γ sheets as being 'electron'-like [58, 59].

Since the surfaces are quasi-two-dimensional the contribution of a single Fermi surface sheet of effective mass m^* to the Sommerfeld coefficient γ can be shown in the case of Sr_2RuO_4 to be [54]

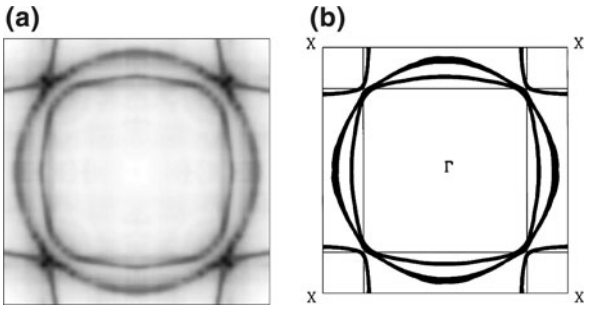

Fig. 2.18 **a** The Sr_2RuO_4 Fermi surface cross section in the k_x–k_y plane of the Brillouin zone as measured by ARPES (graphic reproduced from [31] based on [56]). **b** The same cross section as obtained by LDA calculations [57]. Here the thickness of the lines is indicating the warping of the surfaces in the k_z-direction. Γ labels the zone boundary whereas *X* labels the zone corner

$$\gamma = \frac{\pi N_A k_B^2 a^2}{3\hbar^2} m^*. \tag{2.27}$$

Here, N_A is Avogadro's constant, k_B Boltzmann's constant, $\hbar$ Planck's constant and a the lattice parameter of Sr_2RuO_4. By applying this equation to the measured masses from the de Haas–van Alphen experiments one deduces a total Sommerfeld coefficient of 38.5 mJ/Ru-mol K^2, in good agreement with the value obtained from bulk specific heat measurements.

A further test for the Fermi liquid description of the material is, if the Fermi surface volume can successfully account for all the valence electrons in accordance with Luttinger's theorem [60]. Using the experimental results one obtains a total of 4.05 electrons in the three observed valence bands, in agreement with the four remaining electrons in the Ru^{4+} state of the material.

Overall, one can conclude that the band structure of the normal state of Sr_2RuO_4 can be very well understood in terms of Fermi liquid theory.

2.2.3.2 Fermi Surface of $Sr_3Ru_2O_7$

The Fermi surface structure of Sr_2RuO_4 was discussed in some detail in the previous section because it is a good starting point for understanding the rather more complex Fermi surface structure in $Sr_3Ru_2O_7$.

The first basic assumption for the following line of argument is that in both materials it is the energy bands largely originating from the Ru 4*d* orbitals which cross the Fermi energy. The second assumption is that the change from single layer to double layer material causes a so-called bilayer splitting, i.e. doubling of the number of bands, but does not affect the quasi-two-dimensionality of the Fermi surface. The third assumption is that the rotation of the octahedra in the *ab* plane causes a $\sqrt{2} \times \sqrt{2}$ reconstruction of the unit cell but is otherwise, due to its smallness, only a weak perturbation.

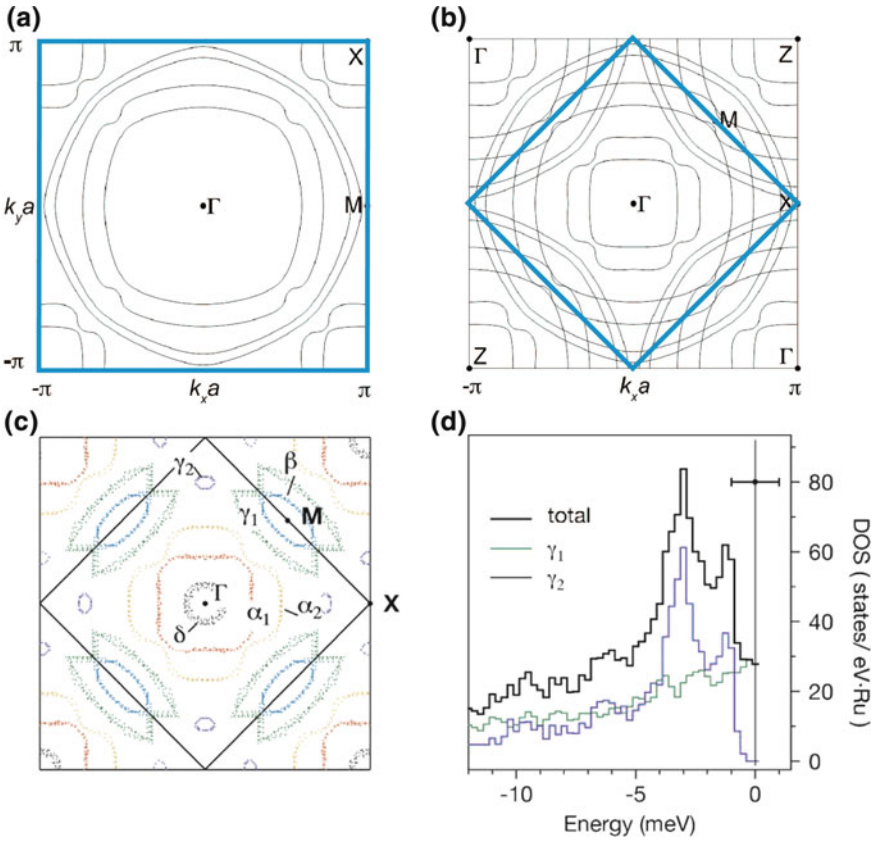

Fig. 2.19 This figure shows schematically how the complex zero field Fermi surface of $Sr_3Ru_2O_7$ can be understood by considering the effects of the differences in structure between the two materials being treatable as perturbations to the band structure. **a** The expected effect of a bi-layer splitting on the Fermi surface. The quasi-two-dimensionality of the Fermi surface is assumed to be retained. If one takes into account the $\sqrt{2} \times \sqrt{2}$ reconstruction of the unit cell due to the rotation of the RuO-octahedra one expects the Brillouin zone to halve and rotate by 45°. This new Brillouin zone is shown in *blue* in **b**. The bands have to be folded into this new zone as indicated. This results in a high degeneracy in the band structure along certain paths in momentum space. These are lifted, leading to a reconstruction of the Fermi surface. **c** The band structure in the k_x–k_y plane as extracted from an ARPES measurement [61]. For details regarding the labelling please see text. **d** The density of states as function of energy relative to the Fermi energy as measured by ARPES for the two γ pockets and their total sum. The error bar in energy represents the experimental uncertainty in the position of the Fermi energy. The plot is reproduced from [61] (labelling changed for consistency)

The effect of these assumptions on the Fermi surface are sketched in Fig. 2.19a and b which are reproduced from [37]. Part (a) shows the k_x–k_y plane of the Sr_2RuO_4 Brillouin zone. Here the previously presented Fermi surfaces are shown doubled due to the bilayer splitting. In part (b) the new Brillouin zone due to the

$\sqrt{2} \times \sqrt{2}$ reconstruction of the unit cell is shown in blue. The bands are 'back-folded' resulting in the shown complex Fermi surface topology.

If one would stop the 'Gedanken experiment' here, then the eigenenergies of the resulting bands would be degenerate along several paths in momentum space. Perturbation theory predicts that in a material these degeneracies are lifted. This in turn would lead to a reconnection of the Fermi surface which in its details is sensitive to the exact prevailing energetics in the material. Figure 2.19c shows the Fermi surface in the k_x–k_y plane as extracted from an ARPES measurements by Tamai et al. [61]. Though different in detail, the overall geometrical similarities between the measurement and the prediction based on a very simple model is remarkable. One can therefore assume as an hypothesis that the above assumptions are a good starting point for an understanding of the band structure of $Sr_3Ru_2O_7$ in zero field. The Fermi surfaces in Fig. 2.19c are therefore labelled in accordance to their relation to the Fermi surface and band structure in Sr_2RuO_4. For example the α_1 and α_2 sheets are mainly derived from the α Fermi surface sheet in Sr_2RuO_4. One obvious difference to the Fermi surface as expected from the simple model presented earlier is the additional δ-surface centred at the Γ point of the Brillouin zone. LDA calculations by Singh [61] indicate that this pocket is derived from a band that did not cross the Fermi energy in Sr_2RuO_4 but also has primarily a Ru $4d$ orbital character (in this case $d_{x^2-y^2}$). Overall, the ARPES measurement observed five sheets that certainly cross the Fermi energy, namely α_1, α_2, β, γ_1 and δ. LDA calculations indicate that δ is indeed bilayer split but that the splitting could not be resolved. The sixth Fermi surface shown, γ_2 is particular in that the energy resolution of the ARPES measurement is not sufficient in its own in order to decide if this pocket is indeed crossing the Fermi energy or is situated just below it. However, the γ_2 surface proves to be critical to the properties of the material. First of all if one excludes it then the observed Fermi surface can only account for $\approx$40% of the total measured specific heat, as will be discussed in more detail below. Secondly ARPES measurements of the band structure below the Fermi energy revealed two peaks in the density of states $g(\epsilon)$ of the γ_2 pocket. This is shown in Fig. 2.19d (the graph is reproduced from [61] with alterations to the labelling for consistency). Here the density of states (DOS) of the two γ pockets and the total sum is shown as a function of energy relative to the Fermi energy. A small peak is situated at ≈ -1 meV and a stronger one related to a saddle point in the band structure at ≈ -4 meV. The error bar shows the uncertainty in the determination of the position of the Fermi energy in the experiment.

The detailed properties of these six Fermi surfaces will be presented at the end of this section together with the results from de Haas–van Alphen measurements. Quantum oscillations in resistivity (Shubnikov–de Haas effect) and magnetic susceptibility (de Haas–van Alphen measurements) in $Sr_3Ru_2O_7$ have been reported in several papers [62, 63]. The most detailed study on the samples with the highest purity has been performed recently by Mercure et al. [37]. On the low field side, with magnetic field applied parallel to the crystallographic c-axis, they were able to observe the same five Fermi surface sheets as the ARPES measurements, namely α_1,

Table 2.1 The properties of the $Sr_3Ru_2O_7$ Fermi surfaces as measured by de Haas–van Alphen (dHvA) and ARPES experiments

	α_1	α_2	β	γ_1	γ_2	δ
dHvA						
F (kT)	1.78	4.13	0.15	0.91	–	0.43
Area (% BZ)	13.0	30.1	1.09	6.64	–	3.14
m^* (m_e)	6.9 ± 0.1	10.1 ± 0.1	5.6 ± 0.3	7.7 ± 0.3	–	8.4 ± 0.7
ARPES						
Area (% BZ)	14.1	31.5	2.6	8.0	<1	2.1
m^* (m_e)	8.6 ± 3	18 ± 8	4.3 ± 2	9.6 ± 3	10 ± 4	8.6 ± 3

F is the observed frequency in $1/H$ of quantum oscillations, BZ stands for Brillouin zone and m^* is the effective mass in units of electron mass m_e. Reproduced from [37]

α_2, β, γ_1 and δ. The angular dependence of the oscillations is consistent with these Fermi surface pockets being quasi-two-dimensional.

The amplitude of the extremely small γ_2 pocket was not identified in the initial de Haas–van Alphen measurements performed in the study. For the other five pockets both the cross-sectional area and the effective mass were measured with relatively high accuracy. Table 2.1 reproduced from [37] gives the detailed results as obtained from both measurements

The overall agreement between the two measurements is good with the de Haas–van Alphen results showing the smaller experimental uncertainty. An important test is if these measurements can explain the experimentally observed bulk specific heat. If one takes only the five Fermi surfaces excluding γ_2 into account than the expected Sommerfeld coefficient from the de Haas–van Alphen experiment is (56 ± 1) mJ/Ru-mol K^2 and from the ARPES measurements (67 ± 12) mJ/Ru-mol K^2, both of which account for only approximately half of the measured specific heat value of 110 mJ/Ru-mol K^2.

The γ_2 pocket on the other hand occurs four times in the Brillouin zone and furthermore is probably bilayer split. The contribution to the Sommerfeld coefficient is therefore eight times the value as calculated based on its effective mass m^* alone. Taking the mass of the γ_2 pocket as measured by ARPES into account would therefore result in revised estimates of the Sommerfeld coefficient of (127 ± 27) mJ/Ru-mol K^2 (ARPES) and (116 ± 16) mJ/Ru-mol K^2 (de Haas–van Alphen). These values would be in broad agreement with the specific heat measurements. Since the size of the γ_2 is negligible on the scale of the size of the Brillouin zone it has a very small effect on the Luttinger sum for the total number of electrons enclosed by the Fermi surfaces.

Contrary to ARPES, the de Haas–van Alphen effect is intrinsically suited to extend the Fermi surface study to high magnetic fields. Here I will summarize the main findings by Mercure et al. [37] as relevant to this thesis.

1. One of the most important results is the absence of any significant effective mass increase in the vicinity of the critical field for any of the five observed frequencies. Figure 2.20a shows this as an example for three of the observed

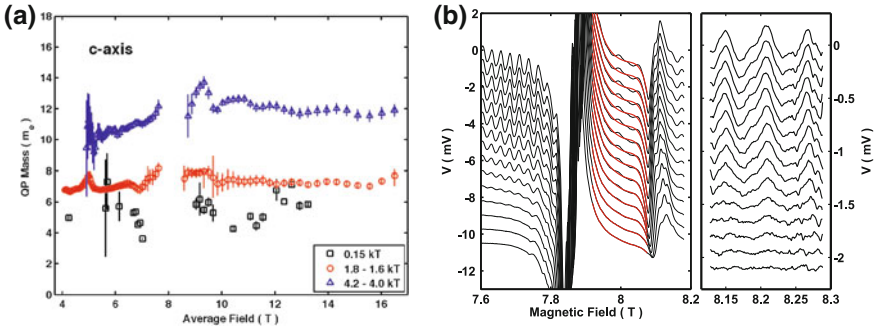

Fig. 2.20 **a** The quasiparticle mass as a function of magnetic field for some of the frequencies observed by de Haas–van Alphen measurements. **b** Data of second harmonic de Haas–van Alphen measurements. The traces which correspond to different sample temperatures have been offset for clarity. In the *right panel* the data inside the novel quantum phase are shown after the background given in *red* in the *left panel* has been subtracted (graphics courtesy of J.-F. Mercure). For more details see [37]

frequencies. Here the effective quasiparticle (QP) mass is plotted as a function of magnetic field applied parallel to the c-axis of $Sr_3Ru_2O_7$. Therefore, the specific heat contribution of the five Fermi surface sheets α_1, α_2, β, γ_1 and δ cannot explain the observed peak in the A-coefficient of resistivity as discussed in the previous section.

2. Mercure et al. succeeded in measuring quantum oscillations in the region of the new phase as shown in Fig. 2.20b. The left panel shows the second harmonic of an AC magnetic susceptibility measurement as a function of magnetic field for several temperatures. Here the traces have been offset in order of temperature for clarity and the upmost trace corresponds to the lowest temperature. The two strong features correspond to the phase boundaries of the novel phase and the red curves are a polynomial background fit to the data. The right panel shows the data with this background being subtracted. Here the quantum oscillations are clearly identifiable. The phase of the oscillations has no apparent temperature dependence. Furthermore the amplitude dependence on temperature is well described by the Lifshitz–Kosevich formula. One can conclude that at least part of the excitation spectrum in the novel quantum phase is therefore consistent with the existence of Fermi liquid quasiparticles. That does not mean however that all electronic degrees of freedom can necessarily be described as itinerant quasiparticles, with other examples where this is considered to be a possibility being high-T_C superconductors [64] and heavy Fermion Kondo systems [22].
3. The observed frequency structure in the high field Fermi liquid state is highly fractured and the amplitude significantly suppressed. Possible reasons for this can be magnetic breakdown and Fermi surface reconstruction.

The ARPES and de Haas–van Alphen measurements presented here therefore seem to indicate that the physics of $Sr_3Ru_2O_7$ is driven by a single band of the complicated band structure which is associated with the γ_2 pocket. It has to be

emphasized that this conclusion is reached by elimination of the remaining Fermi surface and the evidence for a peak in the single-particle density of states associated with γ_2. No direct evidence of the field dependence of this peak or the effective mass of γ_2 exists.

Within the above assumptions only one of the Fermi surfaces would have a significantly field dependent effective mass. In this case the resistivity of only one Fermi surface would show a peak as a function of magnetic field. A commonly raised concern is that this peak should in a simple model not dominate the overall resistance since the conductance channels of all Fermi surface sheets add in parallel. This is seemingly at odds with the results by Grigera et al. [34], where a significant increase of at least a factor of 5 was observed in the A coefficient of the temperature dependent part of the resistivity as a function of magnetic field. However, one has to keep in mind that Grigera et al. have measured the A coefficient of the *magneto*-resistance of $Sr_3Ru_2O_7$. Therefore, one has to take into account that it is not the scalar longitudinal magnetoresistance of the Fermi surfaces but the full resistivity tensor that is added in parallel in order to calculate the overall resistivity of the material as discussed in Sect. 2.1.3.[7] Under these conditions it is possible that the divergence in the resistivity in one of the Fermi surfaces is dominating the total resistivity over a wide field range.

2.3 Summary

In this chapter I discussed the general framework of Fermi liquid theory as well as the concepts of quantum criticality and 'electron-nematic' transport. I furthermore reviewed the experimental evidence for a quantum critical end point in the material as well as thermodynamic measurements of a novel quantum phase in its vicinity which shows features of electron nematic like properties in transport measurements. I finally discussed the current knowledge of the zero field Fermi surface and the extent to which measured quasiparticle observations can account for the observed thermodynamic behaviour.

In this thesis several open questions arising from the current available experimental data will be addressed by magnetothermal studies and specific heat measurements.

[7] It has to be noted here that the simple addition of the resistivity tensors only holds for closed Fermi surfaces. If open orbits are present, the longitudinal magnetoresistance does not only depend on the magnitude of the applied magnetic field but also crucially on the orientation between the electric field and the open orbit, leading to significant anisotropies in transport. Intriguingly, if domains of different orbital orientations exist in the anomalous phase region that are orientable by a small in-plane magnetic field one would naturally expect 'nematik-like' transport properties similar to the ones observed by Borzi et al. To the authors best knowledge though discussed in private communications this path has not been explored in the theoretical literature so far.

The first part of the project is to investigate the entropic properties of the supposed low and high field Fermi liquid states. In particular the question of a peak in the Sommerfeld coefficient that was indirectly inferred from the measured peak in the A coefficient will be discussed. Furthermore data will be presented on magnetothermal oscillations, quantum oscillations in the entropy which can be studied by a method that is particularly sensitive to low frequencies.

The second part of the project relates to the novel quantum phase. Here the main data that will be presented will concern the nature of the surrounding phase transitions as well as the temperature dependence of the specific heat inside the phase.

References

1. Landau LD (1956) The theory of a Fermi liquid. JETP 30:1058
2. Landau LD (1957) Oscillations in a Fermi liquid. JETP 32:59
3. Landau LD (1958) On the theory of a Fermi liquid. JETP 35:97
4. Bednorz JG, Müller KA (1986) Possible high-T_c superconductivity in the Ba–La–Cu–O system. Z Phys B Condens Matter 64(2):189–193
5. Kamihara Y, Watanabe T, Hirano M, Hosono H (2008) Iron-based layered superconductor La[$O_{1-x}F_x$]FeAs ($x = 0.05 - 0.12$) with $T_c = 26$ K. J Am Chem Soc 130(11):3296–3297
6. Ashcroft NW, Mermin ND (1976) Solid state physics. Saunders, Philadelphia
7. Abrikosov AA, Gorkov LP, Dzyaloshinski IE (1975) Methods of quantum field theory in statistical physics. Dover, New York
8. The fermi surface data base (2009). http://www.phys.ufl.edu/fermisurface/jpg/Cu.jpg
9. Choy T-S, Naset J, Chen J, Hershfield S, Stanton C (2000) A database of fermi surface in virtual reality modeling language (vrml). Bulletin of the American Physical Society, vol 45, p L36.42
10. Shoenberg D (1984) Magnetic oscillations in metals. Cambridge University Press, Cambridge
11. Onsager L (1952) Philos Mag 43:1006
12. Pippard AB (1965) The dynamics of conduction electrons. Blackie, Glasgow
13. Kadowaki K, Woods SB (1986) Universal relationship of the resistivity and specific-heat in heavy-Fermion compounds. Solid State Commun 58(8):507–509
14. Hussey NE (2005) Non-generality of the Kadowaki–Woods ratio in correlated oxides. J Phys Soc Jpn 74(4):1107–1110
15. Landau LD (1960) Theoretical physics in the twentieth century, a memorial volume to Wolfgang Pauli. Interscience, NY, 245 pp
16. Kohn W, Luttinger JM (1965) New mechanism for superconductivity. Phys Rev Lett 15:524
17. Doiron-Leyraud N, Proust C, LeBoeuf D, Levallois J, Bonnemaison J-B, Liang R, Bonn DA, Hardy WN, Taillefer L (2007) Quantum oscillations and the Fermi surface in an underdoped high-T_c superconductor. Nature 447(7144):565–568
18. Sebastian SE, Harrison N, Palm E, Murphy TP, Mielke CH, Liang R, Bonn DA, Hardy WN, Lonzarich GG (2008) A multi-component Fermi surface in the vortex state of an underdoped high-T_c superconductor. Nature 454(7201):200–203
19. Vignolle B, Carrington A, Cooper RA, French MMJ, Mackenzie AP, Jaudet C, Vignolles D, Proust C, Hussey NE (2008) Quantum oscillations in an overdoped high-T_c superconductor. Nature 455(7215):952–955
20. Tsui DC, Störmer HL, Gossard AC (1982) Two-dimensional magnetotransport in the extreme quantum limit. Phys Rev Lett 48(22):1559–1562

21. Stewart GR (2001) Non-Fermi-liquid behavior in *d*- and *f*-electron metals. Rev Mod Phys 73(4):797–855
22. Löhneysen Hv, Rosch A, Vojta M, Wölfle P (2007) Fermi-liquid instabilities at magnetic quantum phase transitions. Rev Mod Phys 79(3):1015–1075
23. Gegenwart P, Si Q, Steglich F (2008) Quantum criticality in heavy-fermion metals. Nat Phys 4(3):186–197
24. Grigera SA, Mackenzie AP, Schofield AJ, Julian SR, Lonzarich GG (2002) A metamagnetic quantum critical endpoint in $Sr_3Ru_2O_7$. Int J Modern Phys B 16(20–22):3258–3264 (4th conference on physical phenomena at high magnetic fields, Santa FE, New Mexico, 19–25 October 2001)
25. Custers J, Gegenwart P, Wilhelm H, Neumaier K, Tokiwa Y, Trovarelli O, Geibel C, Steglich F, Pepin C, Coleman P (2003) The break-up of heavy electrons at a quantum critical point. Nature 424(6948):524–527
26. Mathur ND, Grosche FM, Julian SR, Walker IR, Freye DM, Haselwimmer RKW, Lonzarich GG (1998) Magnetically mediated superconductivity in heavy Fermion compounds. Nature 394(6688):39–43
27. Hertz JA (1976) Quantum critical phenomena. Phys Rev B 14(3):1165–1184
28. Millis AJ (1993) Effect of a nonzero temperature on quantum critical-points in itinerant Fermion systems. Phys Rev B 48(10):7183–7196
29. Maeno Y, Hashimoto H, Yoshida K, Nishizaki S, Fujita T, Bednorz JG, Lichtenberg F (1994) Superconductivity in a layered perovskite without copper. Nature 372(6506):532–534
30. Rice TM, Sigrist M (1995) Sr_2RuO_4 - an electronic analog of ^{3}He. J Phys Condens Matter 7(47):L643–L648
31. Mackenzie AP, Maeno Y (2003) The superconductivity of Sr_2RuO_4 and the physics of spin-triplet pairing. Rev Mod Phys 75(2):657–712
32. Ikeda S, Maeno Y, Nakatsuji S, Kosaka M, Uwatoko Y (2000) Ground state in $Sr_3Ru_2O_7$: Fermi liquid close to a ferromagnetic instability. Phys Rev B 62(10):R6089–R6092
33. Vollhardt D (1984) Normal ^{3}He—an almost localized Fermi-liquid. Rev Mod Phys 56(1):99–124
34. Grigera SA, Perry RS, Schofield AJ, Chiao M, Julian SR, Lonzarich GG, Ikeda SI, Maeno Y, Millis AJ, Mackenzie AP (2001) Magnetic field-tuned quantum criticality in the metallic ruthenate $Sr_3Ru_2O_7$. Science 294(5541):329–332
35. Grigera SA, Gegenwart P, Borzi RA, Weickert F, Schofield AJ, Perry RS, Tayama T, Sakakibara T, Maeno Y, Green AG, Mackenzie AP (2004) Disorder-sensitive phase formation linked to metamagnetic quantum criticality. Science 306(5699):1154–1157
36. Borzi RA, Grigera SA, Farrell J, Perry RS, Lister SJS, Lee SL, Tennant DA, Maeno Y, Mackenzie AP (2007) Formation of a nematic fluid at high fields in $Sr_3Ru_2O_7$. Science 315(5809):214–217
37. Mercure J-F (2008) The de Haas–van Alphen effect near a quantum critical end point in $Sr_3Ru_2O_7$. PhD Thesis, September 2008
38. Chmaissem O, Jorgensen JD, Shaked H, Ikeda S, Maeno Y (1998) Thermal expansion and compressibility of Sr_2RuO_4. Phys Rev B 57(9):5067–5070
39. Huang Q, Lynn JW, Erwin RW, Jarupatrakorn J, Cava RJ (1998) Oxygen displacements and search for magnetic order in $Sr_3Ru_2O_7$. Phys Rev B 58(13):8515–8521
40. Kiyanagi R, Tsuda K, Aso N, Kimura H, Noda Y, Yoshida Y, Ikeda S-I, Uwatoko Y (2004) Investigation of the structure of single crystal $Sr_3Ru_2O_7$ by neutron and convergent beam electron diffractions. J Phys Soc Jpn 73(3):639–642
41. Cao G, McCall S, Crow JE (1997) Observation of itinerant ferromagnetism in layered $Sr_3Ru_2O_7$ single crystals. Phys Rev B 55(2):R672–R675
42. Ikeda SI, Maeno Y (1999) Magnetic properties of bilayered $Sr_3Ru_2O_7$. Phys B 261:947–948 (international conference on strongly correlated electron systems (SCES 98), Paris, France, 15–18 July 1998)
43. Perry RS, Maeno Y (2004) Systematic approach to the growth of high-quality single crystals of $Sr_3Ru_2O_7$. J Cryst Growth 271(1–2):134–141

44. Perry RS, Galvin LM, Grigera SA, Capogna L, Schofield AJ, Mackenzie AP, Chiao M, Julian SR, Ikeda SI, Nakatsuji S, Maeno Y, Pfleiderer C (2001) Metamagnetism and critical fluctuations in high quality single crystals of the bilayer ruthenate $Sr_3Ru_2O_7$. Phys Rev Lett 86(12):2661–2664
45. Stryjewski E, Giordano N (1977) Metamagnetism. Adv Phys 26:487
46. Grigera SA, Borzi RA, Mackenzie AP, Julian SR, Perry RS, Maeno Y (2003) Angular dependence of the magnetic susceptibility in the itinerant metamagnet $Sr_3Ru_2O_7$. Phys Rev B 67(21):214427
47. Millis AJ, Schofield AJ, Lonzarich GG, Grigera SA (2010) Metamagnetic quantum criticality in metals. Phys Rev Lett 88(21):217204
48. Zhu LJ, Garst M, Rosch A, Si QM (2003) Universally diverging Grüneisen parameter and the magnetocaloric effect close to quantum critical points. Phys Rev Lett 91(6)
49. Berridge AM, Green AG, Grigera SA, Simons BD (2008) Inhomogeneous magnetic phases: a LOFF-like phase in $Sr_3Ru_2O_7$. Phys Rev Lett (accepted). arXiv:0810.2096v1
50. Gegenwart P, Weickert F, Garst M, Perry RS, Maeno Y (2006) Metamagnetic quantum criticality in $Sr_3Ru_2O_7$ studied by thermal expansion. Phys Rev Lett 96(13):136402
51. Nishizaki S, Maeno Y, Mao ZQ (2000) Changes in the superconducting state of Sr_2RuO_4 under magnetic fields probed by specific heat. J Phys Soc Jpn 69(2):572–578
52. Mackenzie AP, Ikeda S, Maeno Y, Fujita T, Julian SR, Lonzarich GG (1998) Fermi surface topography of Sr_2RuO_4. J Phys Soc Jpn 67(2):385–388
53. Bergemann C, Julian SR, Mackenzie AP, NishiZaki S, Maeno Y (2000) Detailed topography of the Fermi surface of Sr_2RuO_4. Phys Rev Lett 84(12):2662–2665
54. Mackenzie AP, Julian SR, Diver AJ, McMullan GJ, Ray MP, Lonzarich GG, Maeno Y, Nishizaki S, Fujita T (1996) Quantum oscillations in the layered perovskite superconductor Sr_2RuO_4. Phys Rev Lett 76(20):3786–3789
55. Bergemann C, Mackenzie AP, Julian SR, Forsythe D, Ohmichi E (2003) Quasi-two-dimensional Fermi liquid properties of the unconventional superconductor Sr_2RuO_4. Adv Phys 52(7):639–725
56. Damascelli A, Lu DH, Shen KM, Armitage NP, Ronning F, Feng DL, Kim C, Shen ZX, Kimura T, Tokura Y, Mao ZQ, Maeno Y (2000) Fermi surface, surface states, and surface reconstruction in Sr_2RuO_4. Phys Rev Lett 85(24):5194–5197
57. Mazin II, Singh DJ (1997) Ferromagnetic spin fluctuation induced superconductivity in Sr_2RuO_4. Phys Rev Lett 79(4):733–736
58. Shen KM, Kikugawa N, Bergemann C, Balicas L, Baumberger F, Meevasana W, Ingle NJC, Maeno Y, Shen Z-X, Mackenzie AP (2007) Evolution of the Fermi surface and quasiparticle renormalization through a van Hove singularity in $Sr_{2-y}La_yRuO_4$. Phys Rev Lett 99(18):187001
59. Kikugawa N, Mackenzie AP, Bergemann C, Borzi RA, Grigera SA, Maeno Y (2004) Rigid-band shift of the Fermi level in the strongly correlated metal: $Sr_{2-y}La_yRuO_4$. Phys Rev B 70(6):060508
60. Luttinger JM (1960) Fermi surface and some simple equilibrium properties of a system of interacting Fermions. Phys Rev 119(4):1153–1163
61. Tamai A, Allan MP, Mercure JF, Meevasana W, Dunkel R, Lu DH, Perry RS, Mackenzie AP, Singh DJ, Shen Z-X, Baumberger F (2008) Fermi surface and van Hove singularities in the itinerant metamagnet $Sr_3Ru_2O_7$. Phys Rev Lett 101(2):026407
62. Perry RS, Kitagawa K, Grigera SA, Borzi RA, Mackenzie AP, Ishida K, Maeno Y (2004) Multiple first-order metamagnetic transitions and quantum oscillations in ultrapure $Sr_3Ru_2O_7$. Phys Rev Lett 92(16):166602
63. Borzi RA, Grigera SA, Perry RS, Kikugawa N, Kitagawa K, Maeno Y, Mackenzie AP (2004) de Haas–van Alphen effect across the metamagnetic transition in $Sr_3Ru_2O_7$. Phys Rev Lett 92(21):216403
64. Damascelli A, Hussain Z, Shen ZX (2003) Angle-resolved photoemission studies of the cuprate superconductors. Rev Mod Phys 75(2):473–541

http://www.springer.com/978-3-642-14523-0

Magnetothermal Properties near Quantum Criticality in the Itinerant Metamagnet Sr3Ru2O7

Rost, A.W.

2010, X, 145 p., Hardcover
ISBN: 978-3-642-14523-0